

Learning Subgrid-Scale Models in Discontinuous Galerkin Methods with Neural Ordinary Differential Equations for Compressible Navier–Stokes Equations

Shinhoo Kang^{a,*}, Emil M. Constantinescu^a

^a*Mathematics and Computer Science Division, Argonne National Laboratory, Lemont, IL 60439, USA.*

Abstract

The growing computing power over the years has enabled simulations to become more complex and accurate. However, high-fidelity simulations, while immensely valuable for scientific discovery and problem solving, come with significant computational demands. As a result, it is common to run a low-fidelity model with a subgrid-scale model to reduce the computational cost, but selecting the appropriate subgrid-scale models and tuning them are challenging. We propose a novel method for learning the subgrid-scale model effects when simulating partial differential equations using neural ordinary differential equations in the context of discontinuous Galerkin (DG) spatial discretization. Our approach learns the missing scales of the low-order DG solver at a continuous level and hence improves the accuracy of the low-order DG approximations as well as accelerates the filtered high-order DG simulations with a certain degree of precision. We demonstrate the performance of our approach through multidimensional Taylor–Green vortex examples at different Reynolds numbers and times, which cover laminar, transitional, and turbulent regimes. The proposed method not only reconstructs the subgrid-scale from the low-order (1st-order) approximation but also speeds up the filtered high-order DG (6th-order) simulation by two orders of magnitude.

Keywords: neural ordinary differential equations, machine learning, acceleration, turbulence, Navier–Stokes equations, discontinuous Galerkin

1. Introduction

High-order discontinuous Galerkin (DG) methods have received great attention in solving partial differential equations arising from many scientific and engineering problems due to their high-order accuracy and efficiency in modern computing architectures [1, 2, 3, 4, 5, 6, 7]. However, it is still challenging to solve practical problems such as blood flows, atmospheric and ocean currents, wildfires, and wind turbines because of their multiscale nature. Resolving all scales is computationally infeasible. As a result, physical modeling is typically carried out on a coarse grid using the appropriate subgrid-scale (SGS) models. For example, large eddy simulation (LES) resolves large-scale turbulence motion on a grid, which carries most of the flow energy, while modeling the small scales, which have relatively little influence on the mean flow [8].

The goal of SGS models is to capture the effect of the small-scale structures that cannot be resolved in the grid on the resolved scales and to guarantee numerical stability [9]. The static Smagorinsky model [10] and dynamic Smagorinsky model [11], which predict the dissipation of SGS energy, are the most widely used SGS models for turbulence. In high-order DG methods, both Collis [12] and Sengupta et al. [13] successfully used the static Smagorinsky model and dynamic Smagorinsky model, respectively. However, these Smagorinsky models perform poorly for certain flows [14, 15] because they are based on the eddy viscosity assumption that is always purely dissipative and thus are unable to account for energy flow from small scales to large scales (backscatter) [16, 11].

Alternatively, numerical dissipation can be used for modeling unresolved scales as an implicit SGS model. Implicit LES has emphasized the significance of selecting numerical methods rather than modeling missing physics explicitly,

*Corresponding author

Email addresses: shinhoo.kang@anl.gov (Shinhoo Kang), emconsta@anl.gov (Emil M. Constantinescu)

and it has been widely adopted by the community due to its simplicity. In particular, finite volume or DG methods already have the localized built-in stabilization mechanism via numerical flux. Boris [17] exploited the leading-order dissipation term introduced by a numerical upwinding scheme in finite volume methods. Uranga et al. [18] chose high-order DG methods combined with diagonally implicit Runge–Kutta schemes for simulating the transition to turbulence at low Reynolds numbers. Gassner and Beck [19] examined the applicability of very high-order DG approximation with explicit Runge–Kutta methods and proper stabilization (e.g., the exponential-based modal filter [20] and overintegration) for the simulation of underresolved turbulent flows. However, high-order polynomial approximation considerably increases the degrees of freedom and thus the computing cost in three-dimensional problems [7].

Combining computational fluid dynamics and machine learning methods can provide new perspectives on devising SGS models. Neural networks have already shown their potential applicability as a complement to traditional computational fluid dynamics methods [21, 22, 23]. Vinuesa and Brunton [22] suggested possible enhancements of fluid simulations using neural networks. Kochkov et al. [24] demonstrated how deep learning improves the accuracy of fluid simulations on a coarse grid for 2D turbulence. Duraisamy [25] reviewed machine learning (ML) to augment Reynolds-averaged Navier–Stokes and LES models. Fukami et al. [26] presented a supervised ML method to recover fine-resolution turbulent flows from coarse-resolution flow data in space and time. Beck et al. [27] proposed data-driven closure through supervised learning by constructing a map from direct numerical simulation data and LES data. In particular, Lara and Ferrer [28, 29] accelerated high-order DG solver by running a low-order DG solution with correction at every timestep based on supervised learning. Kang and Constantinescu [30] generalized the discrete correction method [28, 29] to the continuous correction method by augmenting continuous neural network source through neural ordinary differential equations (NODEs) [31].

NODEs are a descent approach to extract the dynamics from time series data. This approach can be seen as residual neural networks (ResNets) [32] in the deep limit [33]. In other words, the network parameters are shared by an infinite number of layers inside a NODE. Thus, a NODE is more memory efficient than ResNet [34]. As long as the integration is stable, a NODE can predict a solution at any target time, meaning that it can handle nonuniform samples or missing data in time series [35]. Also, various standard ODE solvers including Dormand–Prince [36] or Runge–Kutta methods can be employed in a NODE. More important, gradients can be computed by an efficient *adjoint sensitivity method* [37]. Numerous encouraging results have been reported. Zhuang et al. [38] performed image classification on the CIFAR10 dataset. Rackauckas et al. [39] identified the missing term in the Lotka–Volterra system. Huang et al. [40] compensated for the temporal discretization error caused by coarse timestep size. Shankar et al. [41] learned an SGS stress tensor for 2D turbulence with graph neural networks.

In our previous work [30] we presented a methodology for learning subgrid-scale models based on neural ordinary differential equations, where the one-dimensional convection-diffusion equation and viscous Burgers’ equations are addressed using DG methods. In this study we extend the approach to 2D/3D compressible Navier–Stokes equations. We exploit NODEs and high-order DG simulation data to learn the missing scales of the low-order DG solver at a continuous level. To that end, we introduce a neural network source term to the governing equations. We develop a differentiable DG model for compressible Navier–Stokes equations on a structured mesh. Then, we train the network parameters through NODEs. The proposed approach learns the continuous source operator for the low-order DG solver, thereby predicting a solution with a timestep size larger than that of the high-order DG solver. This speeds up the high-order DG simulation. Also, the neural network source term enhances the accuracy of the low-order DG approximations. Moreover, as we demonstrated in our previous study, learning the continuous-in-time operator provides consistent prediction accuracy under timestep changes. This feature extends to this study as well.

The paper is organized as follows. We review nodal DG methods, introduce a projection-based reduced-order model, and describe a neural network augmented system in Section 2. Then we present the proposed method in Section 3. In Section 4 we demonstrate the performance of our proposed methodology by using multidimensional Taylor–Green vortex examples. In Section 5 we summarize our current approach and results and discuss limitations and possible future research.

2. Problem Statement and Preliminaries

2.1. Discontinuous Galerkin method

We briefly review nodal discontinuous Galerkin methods [20, 42]. For clear exposition we focus on a one-dimensional system of a hyperbolic equation,

$$\frac{\partial u}{\partial t} + \frac{\partial f(u)}{\partial x} = 0, \text{ on } \Omega \times [0, T], \quad (1)$$

where $u, f \in \mathbb{R}^n$ are conservative variable and physical flux and $(x, t) \in \Omega \times [0, T]$. We partition the domain Ω into N_{el} non-overlapping elements $I_i = [x_{i-\frac{1}{2}}, x_{i+\frac{1}{2}}]$ and define the mesh $\mathcal{T}_h := \cup_{i=1}^{N_{\text{el}}} I_i$ by a finite collection of the elements I_i . We denote the boundary of element I by ∂I . We let $\partial \mathcal{T}_h := \{\partial I : I \in \mathcal{T}_h\}$ be the collection of the boundaries of all elements. For two neighboring elements I^+ and I^- that share an interior interface $e = I^+ \cap I^-$, we denote by q^\pm the trace of their solutions on e . We define \mathbf{n}^- as the unit outward normal vector on the boundary ∂I^- of element I^- , and we define $\mathbf{n}^+ = -\mathbf{n}^-$ as the unit outward normal of a neighboring element I^+ on e . On the interior face e , we define the mean/average operator $\{\mathbf{v}\}$, where \mathbf{v} is either a scalar or a vector quantify, as $\{\mathbf{v}\} := (\mathbf{v}^- + \mathbf{v}^+)/2$, and the jump operator $[[\mathbf{v}]] := \mathbf{v}^+ \cdot \mathbf{n}^+ + \mathbf{v}^- \cdot \mathbf{n}^-$. Let $\mathcal{P}^N(D)$ denote the space of polynomials of degree at most N on a domain D . Next, we introduce discontinuous piecewise polynomial spaces for scalars and vectors of size $k = (d + 2)$ as

$$\begin{aligned} V_h^N(\mathcal{T}_h) &:= \{v \in L^2(\mathcal{T}_h) : v|_I \in \mathcal{P}^N(I), \forall I \in \mathcal{T}_h\}, \\ \mathbf{V}_h^N(\mathcal{T}_h) &:= \{\mathbf{v} \in [L^2(\mathcal{T}_h)]^k : \mathbf{v}|_I \in [\mathcal{P}^N(I)]^k, \forall I \in \mathcal{T}_h\}, \end{aligned}$$

and similar spaces $V_h^N(I)$ and $\mathbf{V}_h^N(I)$ by replacing \mathcal{T}_h with I . Here, d is the d -dimension. We define $(\cdot, \cdot)_I$ as the L^2 -inner product on an element I and $\langle \cdot, \cdot \rangle_{\partial I}$ as the L^2 -inner product on the element boundary ∂I .

Each element I is the image of the reference element $I^* = [-1, 1]$ by an affine map $x = \phi^I(\xi)$. $|J^I| = \det\left(\frac{\partial x}{\partial \xi}\right) = \frac{\Delta x^I}{2}$ is the determinant of a Jacobian of ϕ^I . On each I , a local solution $u^I \in V_h^N(I)$ is approximated by a linear combination of Lagrange basis functions $\ell_j(\xi) = \prod_{i=0, i \neq j}^N \frac{\xi - \xi_i}{\xi_j - \xi_i}$,

$$u^I(\xi, t) = \sum_{j=0}^N u^I(\xi_j, t) \ell_j(\xi_j),$$

where ξ_j is the Legendre Gauss–Lobatto (LGL) points [42].

The DG weak formulation of (1) yields the following: Seek $u \in V_h^N(I)$ such that

$$|J^I| \mathbf{M} \frac{du}{dt} - \mathbf{Q}^T f + \mathbf{E}^T \mathbf{B} f^* = 0 \quad (2)$$

holds for each element $I \in \mathcal{T}_h$. Here, f^* is a numerical flux; $\mathbf{M}_{ij} = (\ell_i(\xi), \ell_j(\xi))_{I^*}$ is a mass matrix; $\mathbf{Q}_{ij} = (\ell_i(\xi), \frac{\partial \ell_j(\xi)}{\partial \xi})_{I^*}$ is an integrated differentiation matrix;

$$\mathbf{E} = \begin{pmatrix} \ell_0(-1) \\ \ell_N(1) \end{pmatrix}, \text{ and } \mathbf{B} = \begin{pmatrix} -1 & 0 \\ 0 & 1 \end{pmatrix}.$$

Now, we rewrite the DG weak formulation in (2) as an explicit ordinary differential equation

$$\frac{du}{dt} = \frac{1}{|J^I|} \mathbf{M}^{-1} (\mathbf{Q}^T f - \mathbf{E}^T \mathbf{B} f^*) =: R(u). \quad (3)$$

2.2. Projection-based reduced-order model

The high-order DG solution $u^H \in V_h^H(\mathcal{T}_h)$ entails expensive computational cost in high resolution due to large degrees of freedom [7]. To reduce the computational cost, we consider a reduced-order model (ROM) based on an elementwise L_2 projection.

We let $u^H \in V_h^H(I)$ and $u^L \in V_h^L(I)$ be the high- and the low-order DG approximations ($H > L$) on I , respectively. For simplicity, we omit the term ‘‘DG’’ from ‘‘DG approximations’’ from now on. We introduce low- and high-order projection operators \mathcal{P}^L and \mathcal{P}^H , respectively, such that projecting the high-order approximation u^H belongs to the low-order space, $\mathcal{P}^L(u^H) \in V_h^L$ and the low-order approximation u^L to the high-order space, $\mathcal{P}^H(u^L) \in V_h^H$. For implementation, we start by the definition of L_2 projection on each element,

$$(u^H - \mathcal{P}^L(u^H), v)_I = 0, \quad \forall v \in V_h^L. \quad (4)$$

Then, we expand the high- and low-order approximations to $u^H(\xi, t) = \sum_{j=0}^H \ell_j^H(\xi) u_j^H(t)$ and $\mathcal{P}^L(u^H)(\xi, t) = \sum_{j=0}^L \ell_j^L(\xi) (\mathcal{P}^L(u^H))_j(t)$ in (4). By taking $v = \ell_i^L(\xi)$ for $i = 0, \dots, L$ in (4), we build the low-order projection matrix $\mathbf{P}^L \in \mathbb{R}^{(L+1) \times (H+1)}$ such that

$$\mathcal{P}^L(u^H) = \underbrace{(\mathbf{M}^L)^{-1}}_{\mathbf{P}^L} \mathbf{C} u^H \quad (5)$$

where $\mathbf{M}_{ij}^L = (\ell_i^L(\xi), \ell_j^L(\xi))_I$ and $\mathbf{C}_{ij} = (\ell_i^L(\xi), \ell_j^H(\xi))_I$. Similarly, by taking $v = \ell_i^H(\xi)$ for $i = 0, \dots, H$ in (6),

$$(u^L - \mathcal{P}^H(u^L), v)_I = 0, \quad \forall v \in V_h^H, \quad (6)$$

we construct the high-order projection matrix $\mathbf{P}^H \in \mathbb{R}^{(H+1) \times (L+1)}$ satisfying

$$\mathcal{P}^H(u^L) = \underbrace{(\mathbf{M}^H)^{-1}}_{\mathbf{P}^H} \mathbf{C}^T u^L \quad (7)$$

with $\mathbf{M}_{ij}^H = (\ell_i^H(\xi), \ell_j^H(\xi))_I$.

Now, we consider (3) for the high-order approximation u^H ,

$$\frac{du^H}{dt} = R^H(u^H). \quad (8)$$

To model the reduced dynamics of (8), we first replace u^H with $\mathbf{P}^H u^L$ and define the residual r by

$$r = \mathbf{P}^H \frac{du^L}{dt} - R^H(\mathbf{P}^H u^L). \quad (9)$$

Then, we require the residual (9) to be orthogonal to $(L+1)$ -dimensional subspace spanned by the row of the low-order projection matrix \mathbf{P}^L ,

$$\mathbf{P}^L r = 0.$$

In other words, we find $u^L \in V_h^L(I)$ such that

$$\mathbf{P}^L \mathbf{P}^H \frac{du^L}{dt} = \mathbf{P}^L R^H(\mathbf{P}^H u^L) \quad (10)$$

holds. We note that (10) is a Petrov–Galerkin projection-based ROM because $(\mathbf{P}^L)^T \neq \mathbf{P}^H$.

Proposition 1. *If the inner products of \mathbf{M}^L , \mathbf{M}^H , and \mathbf{C} in (5) and (7) are integrated by using Gauss quadrature or LGL quadrature rule with $H + 1$ quadrature points, then \mathbf{P}^L is the left inverse of \mathbf{P}^H . That is, $\mathbf{P}^L \mathbf{P}^H = \mathbf{I}_{L+1}$ holds. Here, $\mathbf{I}_{L+1} \in \mathbb{R}^{(L+1) \times (L+1)}$ is the identity matrix.*

Proof. The highest polynomial order of the integrands for \mathbf{M}^L , \mathbf{M}^H , and \mathbf{C} is $2H$. Therefore, it is sufficient to use $(H + 1)$ quadrature points for evaluating the inner products of \mathbf{M}^L , \mathbf{M}^H , and \mathbf{C} . We define Gauss quadrature points and weights by ξ_q and w_q for $q = 0, 1, \dots, H$. We define the interpolation matrices evaluated at the Gauss quadrature points by \mathbf{I}_g^L and \mathbf{I}_g^H satisfying $(\mathbf{I}_g^L)_{qi} = \ell_i^L(\xi_q)$ and $(\mathbf{I}_g^H)_{qj} = \ell_j^H(\xi_q)$, respectively. Here, $i = 0, \dots, L$ and $j = 0, \dots, H$. We note that $\mathbf{I}_g^H \in \mathbb{R}^{(H+1) \times (H+1)}$ is a square matrix and the column vectors are linearly independent; hence, its inverse matrix $(\mathbf{I}_g^H)^{-1}$ exists. We also denote the Gauss weight matrix by $\mathbf{W}_g = \text{diag}(w_0, w_1, \dots, w_H)$.

With the interpolation matrices and the weight matrix, we rewrite the projection matrices as

$$\mathbf{P}^L = (\mathbf{M}^L)^{-1} (\mathbf{I}_g^L)^T \mathbf{W}_g \mathbf{I}_g^H \text{ and } \mathbf{P}^H = (\mathbf{M}^H)^{-1} (\mathbf{I}_g^H)^T \mathbf{W}_g \mathbf{I}_g^L.$$

This yields

$$\begin{aligned} \mathbf{P}^L \mathbf{P}^H &= (\mathbf{M}^L)^{-1} (\mathbf{I}_g^L)^T \mathbf{W}_g \mathbf{I}_g^H (\mathbf{I}_g^H)^{-1} \mathbf{W}_g^{-1} (\mathbf{I}_g^H)^{-T} (\mathbf{I}_g^H)^T \mathbf{W}_g \mathbf{I}_g^L \\ &= (\mathbf{M}^L)^{-1} (\mathbf{I}_g^L)^T \mathbf{W}_g \mathbf{I}_g^L \\ &= (\mathbf{M}^L)^{-1} \mathbf{M}^L = \mathbf{I}_{L+1}. \end{aligned}$$

With the LGL points, $\ell_i^H(\xi_j) = \delta_{ji}$ for $i, j = 0, 1, \dots, H$. The corresponding interpolation matrix \mathbf{I}_g^H becomes an identity matrix \mathbf{I}_{H+1} . The projection matrices can be simplified as

$$\mathbf{P}^L = (\mathbf{M}^L)^{-1} (\mathbf{I}_g^L)^T \mathbf{W}_g \text{ and } \mathbf{P}^H = \mathbf{I}_g^L,$$

which yields

$$\mathbf{P}^L \mathbf{P}^H = (\mathbf{M}^L)^{-1} \mathbf{M}^L = \mathbf{I}_{L+1}.$$

□

From Proposition 1, (10) becomes

$$\frac{du^L}{dt} = \mathbf{P}^L R^H (\mathbf{P}^H u^L). \quad (11)$$

We note that the subspace spanned by the columns of a matrix \mathbf{P}^H is a reduced linear trial manifold. That is, this method builds local reduced bases.

2.3. Neural network augmented system

We consider the low-order polynomial approximation of (3),

$$\frac{du^L}{dt} = R^L(u^L). \quad (12)$$

In order to improve the solution accuracy in (12), the ROM in (11) could be used; however, it still has to access the high-order right-hand side functional R^H . Moreover, two projection matrices \mathbf{P}^L and \mathbf{P}^H are involved.

Alternatively, we think about using high-order solution data. Applying the low-order projection matrix \mathbf{P}^L to (8), we obtain

$$\frac{d\mathbf{P}^L u^H}{dt} = \mathbf{P}^L R^H(u^H). \quad (13)$$

Both u^L and $\mathbf{P}^L u^H$ belong to the same low-order space $V_h^L(I)$. As mentioned in [28], however, the tendency of $\mathbf{P}^L u^H$ in (13) is not the same as that of u^L in (12); in other words, $\frac{d\mathbf{P}^L u^H}{dt} \neq \frac{du^L}{dt}$. We assume that $\mathbf{P}^L u^H$ is the optimal solution in $V_h^L(I)$.

Problem statement

Our goal is to improve the low-order solution accuracy by introducing the neural network source term S_θ to (12),

$$\frac{d\hat{u}^L}{dt} = \mathbf{R}^L(\hat{u}^L) + S_\theta(\hat{u}^L), \quad (14)$$

where \hat{u}^L is the prediction of the low-order solution with the neural network source term S_θ . Hereafter, we call (14) and \hat{u}^L the augmented system and the augmented solution, respectively.

Remark 1. In this study we solve the 2D/3D compressible Navier–Stokes equations in Appendix A. Our goal is to enhance the low-order solution accuracy by solving the augmented system,

$$\frac{d\hat{\mathbf{u}}^L}{dt} = \mathbf{R}^L(\hat{\mathbf{u}}^L) + \mathbf{S}_\theta(\hat{\mathbf{u}}^L), \quad (15)$$

where \mathbf{R}^L is the low-order spatial discretization of (A.1); $\mathbf{u} = (\rho, \rho\varphi_1, \dots, \rho\varphi_d, \rho E)^T$ is the vector of conservative variables; ρ is the density; φ_i is the velocity component in the i th coordinate direction; ρE is the total energy; $\mathbf{u}^L \in \mathbf{V}_h^L(I)$ is the low-order approximation of \mathbf{u} ; and $\hat{\mathbf{u}} \in \mathbf{V}_h^L(I)$ is the augmented solution of \mathbf{u}^L .

3. Method

Although there are other methods such as discrete corrective term [28, 7, 43] for increasing the low-order solution accuracy, this study focuses on learning the neural network source term through NODEs in (14). The subsections that follow provide a detailed explanation.

3.1. Neural network architecture

For $n_i \in \mathbb{N}$, a D -depth feed-forward neural network is the function that maps an input $z^0 \in \mathbb{R}^{n_0}$ to an output $z^D \in \mathbb{R}^{n_D}$, which consists of D network layers,

$$\begin{aligned} z^i &= W^i \sigma(z^{i-1}) + b^i, \quad \text{for } i = 1, 2, \dots, D-1, \\ z^D &= W^D z^{D-1} + b^D. \end{aligned}$$

Here, σ is the rectified linear unit [44] activation functions, with $W^i \in \mathbb{R}^{n_i \times n_{i-1}}$ and $b^i \in \mathbb{R}^{n_i}$ being i th weight matrix and basis vectors. The dimension of the neural network architecture is denoted by $\{n_0, n_1, \dots, n_D\}$.

We exploit two neural network source functions: global and local. A global neural network source function takes the low-order solutions of all the elements and produces a source approximation of all the elements,

$$S_\theta : V_h^L(\mathcal{T}_h) \ni u \rightarrow s \in V_h^L(\mathcal{T}_h), \quad (16)$$

for a scalar equation, and

$$\mathbf{S}_\theta : \mathbf{V}_h^L(\mathcal{T}_h) \ni \mathbf{u} \rightarrow \mathbf{s} \in \mathbf{V}_h^L(\mathcal{T}_h), \quad (17)$$

for a system of equations. For compressible Navier–Stokes equations, the output \mathbf{s} becomes $\mathbf{s} = (s_\rho, s_{\rho u_1}, \dots, s_{\rho u_d}, s_{\rho E})^T$. This global approach can capture the variation of solution in global scale, but the dimensions of the input and the output become too large for multidimensional and high-fidelity simulations. Therefore, we devise a local neural network source function similar to a convolutional kernel.

In a neural network, a convolution is a way to extract features by summarizing an image into fewer pixels. This is done by scanning a convolutional kernel with an $n \times n$ matrix (for $n \in \mathbb{N}$) across the image for each pixel. For DG methods, a local D -depth feed-forward neural network slides over the low-order solutions of all the elements and produces a local source approximation for each element,

$$S_\theta : V_h^L(\mathcal{N}_h(I)) \ni u \rightarrow s \in V_h^L(I), \quad (18)$$

for a scalar equation, and

$$\mathbf{S}_\theta : \mathbf{V}_h^L(\mathcal{N}_h(I)) \ni \mathbf{u} \rightarrow \mathbf{s} \in \mathbf{V}_h^L(I), \quad (19)$$

for a system of equations. Here, $\mathcal{N}_h(I)$ are the adjacent elements of I . For a simple implementation, we focus only on the Cartesian grid. With the analogy of $n \times n$ pixels for an image kernel, we define the adjacent elements by $k_w \times k_w$ elements in a two-dimensional domain, where k_w is the kernel width, meaning the number of elements along an axis in the Cartesian domain. Similarly, the adjacent elements are defined by k_w and $k_w \times k_w \times k_w$ for 1D and 3D domains, respectively. An N th-order scalar solution u of an element has $(N+1)^d$ degrees of freedom. Thus, a local neural source function has $n_0 = (N+1)^d k_w^d$ and $n_D = (N+1)^d$ for the dimensions of the input and the output. For compressible Navier–Stokes systems, we have $n_0 = (N+1)^d k_w^d N_{\text{field}}$ and $n_D = (N+1)^d N_{\text{field}}$ with $N_{\text{field}} = d + 2$.

3.2. Training of neural network source

To obtain the training data, we first generate a single trajectory of high-order solution u^H by solving (8), on which we apply the low-order projection matrix in (5). In training, we randomly select n -batch instances from the trajectory and gather m consecutive instances $\left\{ (\mathbf{P}^L u^H)_{t_s}^{(i)}, (\mathbf{P}^L u^H)_{t_s+\Delta t}^{(i)}, \dots, (\mathbf{P}^L u^H)_{t_s+m\Delta t}^{(i)} \right\}$ for $i = 1, \dots, n$. Here, $(\mathbf{P}^L u^H)_{t_s}^{(i)}$ is the filtered high-order solution at time $t = t_s$ for the i th sample. Next, we predict the augmented solutions with m timesteps by solving (14). Various timestepping schemes can be utilized to integrate (14), but for ease of discussion we confine ourselves to s -stage explicit Runge–Kutta (ERK) schemes with uniform timestep size. Applying ERK schemes to (14) yields

$$\begin{aligned} U_{n,i} &= \hat{u}_n^L + \Delta t \sum_{j=1}^{i-1} a_{ij} (R_j^L + S_{\theta_j}), \quad i = 1, 2, \dots, s, \\ \hat{u}_{n+1}^L &= \hat{u}_n^L + \Delta t \sum_{i=1}^s b_i (R_i^L + S_{\theta_i}), \end{aligned}$$

where $R_i^L := R^L(t_n + c_i \Delta t, U_{n,i})$; $S_{\theta_i} := S_\theta(U_{n,i})$; and a_{ij} , b_i , and c_i are scalar coefficients for s -stage ERK methods. Given an initial condition $(\mathbf{P}^L u^H)_{t_s}^{(i)}$, the m step ERK timestepping method generates m discrete instances for the i th sample, $\left\{ (\hat{u}^L)_{t_s+\Delta t}^{(i)}, (\hat{u}^L)_{t_s+2\Delta t}^{(i)}, \dots, (\hat{u}^L)_{t_s+m\Delta t}^{(i)} \right\}$. We then update the network parameters $\theta = \{W^i, b^i\}_{i=1}^D$ by minimizing the loss,

$$\mathcal{L}(\theta) = \frac{1}{nm} \sum_{i=1}^n \sum_{j=1}^m \left\| (\mathbf{P}^L u^H)_{t_s+j\Delta t}^{(i)} - (\hat{u}^L)_{t_s+j\Delta t}^{(i)} \right\|^2, \quad (20)$$

where $\|\cdot\|^2$ is the mean squared error. For compressible Navier–Stokes systems, the loss becomes

$$\mathcal{L}(\theta) = \frac{1}{nm} \sum_{i=1}^n \sum_{j=1}^m \sum_{k=1}^{N_{\text{field}}} \left\| (\mathbf{P}^L u_k^H)_{t_s+j\Delta t}^{(i)} - (\hat{u}_k^L)_{t_s+j\Delta t}^{(i)} \right\|^2. \quad (21)$$

3.3. Implementation

We develop compressible Navier–Stokes solvers by using the automatic differentiation Python package JAX [45]. We then exploit our proposed approach by using the Optax [46] optimization library, the Equinox [47] neural network libraries, and the Diffrax [48] NODE package. JAX is based on XLA (Accelerated Linear Algebra), which results in significant computing speedups.

For the DG implementation, we use the Lax–Friedrichs flux $f^* = \{f\} + \frac{1}{2} \max \left(\left| \frac{\partial f}{\partial u} \right| \right) \llbracket u \rrbracket$ for inviscid flux and the local discontinuous Galerkin method [49] for viscous flux in (3). For multidimensional problems, we use an inexact mass matrix $\mathbf{M}_{ij} = \delta_{ij} w_i$ with LGL quadrature weights w_i to reduce the computational cost of the mass matrix inversion.

4. Numerical Results

In this section we present numerical results to demonstrate the performance of the proposed approach for learning continuous source dynamics. In all the examples, we have used structured meshes (e.g., quadrilateral elements for 2D and hexahedral elements for 3D) for spatial discretization and uniform timestep size.

4.1. Taylor–Green vortex

The Taylor–Green vortex [50] is an exact solution of two-dimensional, incompressible Navier–Stokes equations. It is widely used for validating the incompressible Navier–Stokes model or compressible Navier–Stokes model at a low Mach number (M_a) regime. In two dimensions, the vortex is stable and maintains its shape, but it will eventually lose energy due to viscous dissipation. In three dimensions, the vortex can stretch and twist in all three spatial dimensions; thus, energy is transported from large scales to smaller scales. This energy cascade allows flow transition from laminar to turbulence. At the smallest scales of turbulence, kinetic energy is dissipated into thermal energy due to viscosity.

The initial field in $\Omega = [-1, 1]^3$ is given by

$$\begin{aligned}\rho &= 1, \\ u &= M_a \sin(\pi x) \cos(\pi y) \cos(\pi z), \\ v &= -M_a \cos(\pi x) \sin(\pi y) \cos(\pi z), \\ w &= 0, \\ p &= \frac{1}{\gamma} + \frac{M_a^2}{16} (\cos(2\pi x) + \cos(2\pi y)) (\cos(2\pi z) + 2).\end{aligned}$$

We take $\gamma = 1.4$ and $Pr = 0.72$. We choose $M_a = 0.1$ so that the flow is in the incompressible flow regime. The initial temperature is computed by $T = \gamma p \rho^{-1}$ from the normalized equation of state. We apply periodic boundary conditions to all the boundaries. For 2D simulation, we remove w , take $z = 0$ for the velocity, and set $p = \frac{1}{\gamma} + \frac{M_a^2}{4} (\cos(2\pi x) + \cos(2\pi y))$.

Two-dimensional vortex

We consider the two-dimensional Taylor–Green vortex for $Re = 100$ on $\Omega = [-1, 1]^2$. We first integrate the high-order model with the third-order ERK scheme and the timestep size of 2×10^{-4} for $t = [0, 1]$ over the mesh of the eight-order polynomial ($N = 8$) and 10×10 elements. Then, we generate the filtered data by applying the projection matrix \mathbf{P}^L in (5) to the conservative variables \mathbf{u}^H on each element at every timestep. Next, we split the time series of $\mathbf{P}^L \mathbf{u}^H$ into the training data for $t = [0, 0.75]$ and the test data for $t = [0.75, 1]$ with the same third-order ERK.

For training the neural network source term, we randomly select two batch instances of $\mathbf{P}^L \mathbf{u}^H$ in the training data and integrate (15) for m timesteps by using the fifth-order ERK method [51] with $\Delta t = 2 \times 10^{-3}$ over the mesh with the first-order $p = 1$ polynomial and 10×10 elements. Since the first-order discontinuous Galerkin methods have four nodal points on each element, the neural network input and output layers in (19) have $n_0 = 16 \times k_w^2$ and $n_D = 16$ degrees of freedom, respectively. We choose the dimension of the neural network source as $\{n_0, 64, 32, 64, n_D\}$. We take the AdaBelief [52] optimizer with a learning rate of 10^{-2} and 500 epochs.

Figure 1 shows the snapshots of the momentum field at $t = 1$ for the filtered solution, the augmented solution, and the low-order solution with $k_w = 5$ and $m = 1$. Both the horizontal and the vertical components of the momentum values are colored in a range of $[-1, 1]$ with 16 intervals. The augmented solutions of $\hat{\rho} u^L$ and $\hat{\rho} v^L$ are closer to the filtered solutions of $\mathbf{P}^L \rho u^H$ and $\mathbf{P}^L \rho v^H$ than the low-order solutions of ρu^L and ρv^L , respectively.

We further perform a sensitivity study with respect to m and k_w , and we plot the relative errors of conservative variables (ρ , $\rho \boldsymbol{\varphi}$, and ρE) at $t = 1$ in Figure 2. Here, $\boldsymbol{\varphi} = (u, v)$. In general, varying m and k_w does not show any significant differences in density, momentum, and total energy. The relative errors of ρ and ρE are within $O(10^{-4})$ and those of $\rho \boldsymbol{\varphi}$ within $O(10^{-2})$. The minimum and the maximum of the relative errors are 4.7×10^{-4} and 8.4×10^{-4} for the density; 1.4×10^{-2} and 3.2×10^{-2} for the momentum; and 3.1×10^{-4} and 4.9×10^{-4} for the total energy.

Since the errors of the momentum are two orders of magnitude larger than the density and the total energy counterparts, we examine the error histories of the conservative variables with $(k_w, m) = (5, 1)$ (which gives the minimum error in the momentum) in Figure 3. The errors of the augmented solution $\hat{\mathbf{u}}^L$ are smaller than those of the low-order

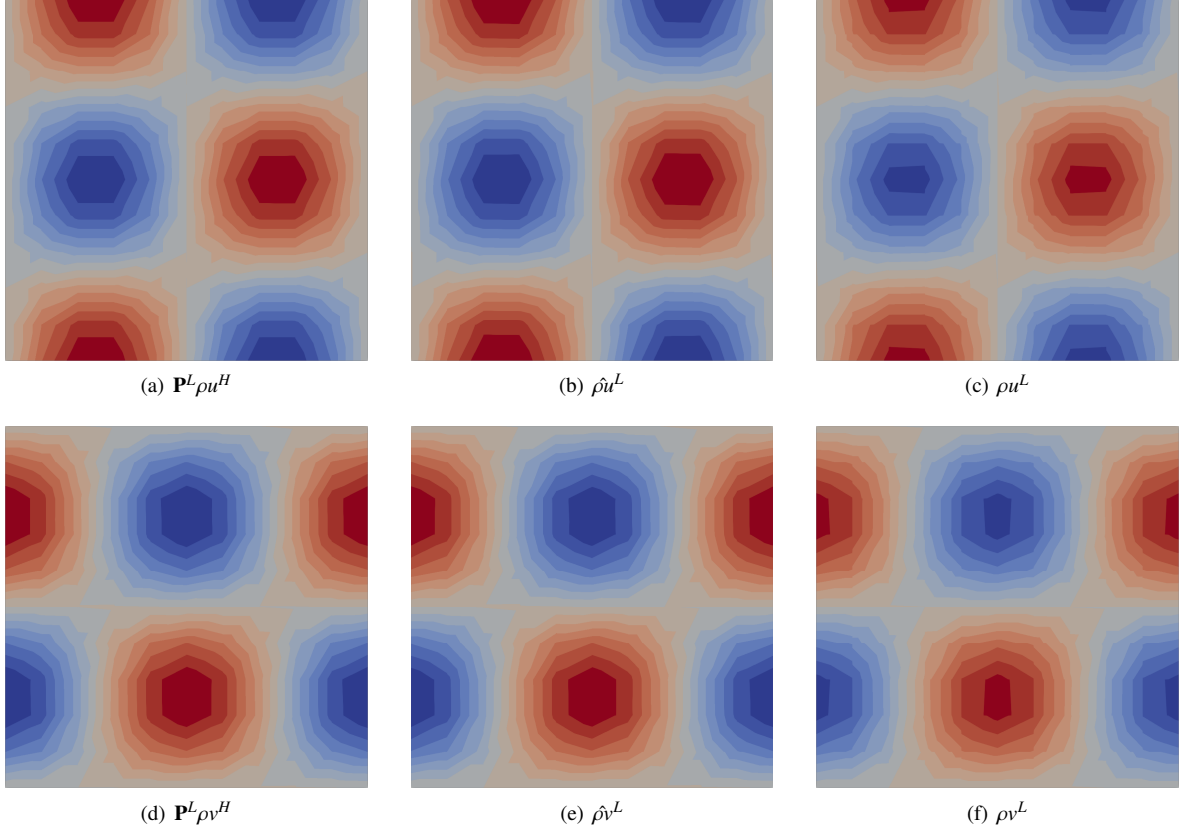


Figure 1: 2D Taylor–Green vortex: snapshots of (a) $\mathbf{P}^L \rho \mathbf{u}^H$, (b) $\hat{\rho} \mathbf{u}^L$, (c) $\rho \mathbf{u}^L$, (d) $\mathbf{P}^L \rho \mathbf{v}^H$, (e) $\hat{\rho} \mathbf{v}^L$, and (f) $\rho \mathbf{v}^L$ with $k_w = 5$ and $m = 1$ at $t = 1$.

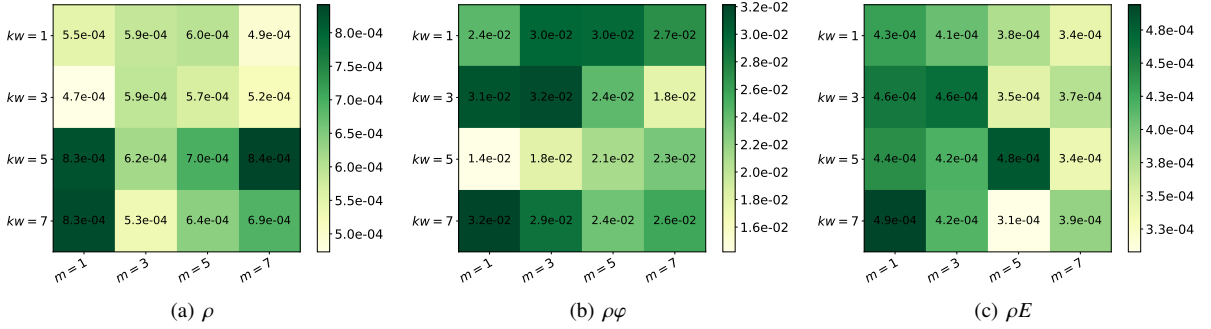


Figure 2: 2D Taylor–Green vortex: relative errors of (a) ρ , (b) $\rho \varphi$, and (c) ρE with respect to kernel width k_w and marching steps m .

solution \mathbf{u}^L for $t \in [0, 1]$. The errors of ρ^L and $\rho \varphi^L$ are three times bigger than those of $\hat{\rho}^L$ and $\hat{\rho} \varphi^L$ at $t = 1$. Similarly, the error of ρE^L is four times higher than $\hat{\rho} E$ counterpart.

Three-dimensional vortex

Next, we consider the three-dimensional Taylor–Green vortex. We integrate the high-order model for third-order ERK with $\Delta t = 10^{-3}$ over the mesh of $10 \times 10 \times 10$ elements ($N_{\text{el}} = 10^3$) and the eight-order polynomial ($N = 8$). Figure 4 shows the evolution of the vortices at $t = \{0, 10, 20\}$ for $Re = 1600$. To visualize the coherent vortical structures in the flow field, we plot Q-criterion isosurfaces with 0.02, which are colored by the z-component of the

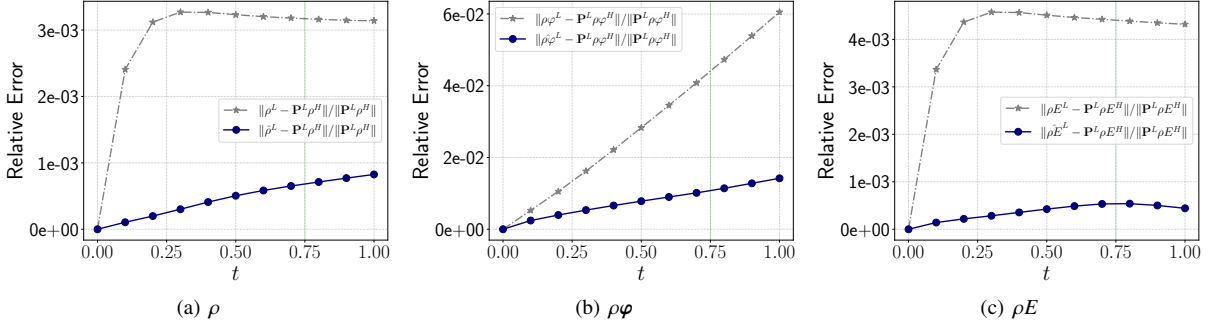


Figure 3: 2D Taylor–Green vortex: error histories of (a) ρ , (b) $\rho\varphi$, and (c) ρE with $k_w = 5$ and $m = 1$.

vorticity from -1 to 1 .¹ The smooth initial vortices are stretched, twisted, and split because of the high Reynolds number, creating turbulent motion. We observe in Figure 5 that the small-scale vortices are generated with increasing Reynolds number.

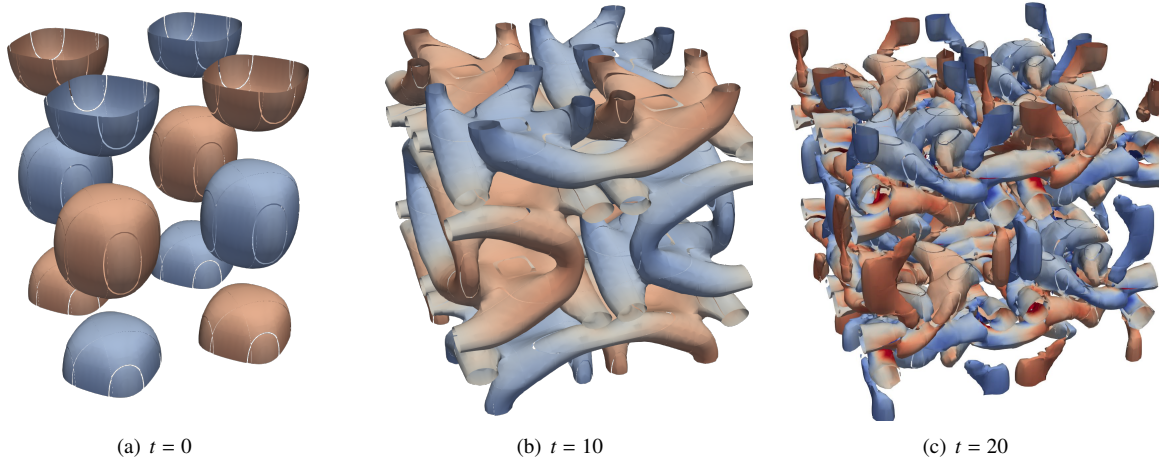


Figure 4: 3D Taylor–Green vortex: Q-criterion isosurfaces for $Re = 1600$ with 10^3 elements and $N = 8$ at (a) $t = 0$, (b) $t = 10$, and (c) $t = 20$. The isosurfaces are colored by the z -component of the vorticity from -1 to 1 .

Based on this observation, we consider 12 datasets with the starting time $t_1 \in \{0, 7, 14\}$ at $Re \in \{100, 200, 400, 1600\}$. Similar to the two-dimensional case, we integrate the high-order model with the third-order ERK scheme and the timestep size of 10^{-3} for one time unit $t \in [t_1, t_1 + 1]$ over the mesh of the sixth-order polynomial ($N = 6$) and $20 \times 20 \times 20$ ($N_{el} = 8000$) elements. We use the projection matrix \mathbf{P}^L in (5) to obtain the filtered data, and we split the time series of $\mathbf{P}^L \mathbf{u}^H$ into the training data for $t = [t_1, t_1 + \frac{3}{4}]$ and the test data for $t = [t_1 + \frac{3}{4}, t_1 + 1]$. We train 12 neural network source terms with each dataset. For training a neural network source term, we randomly select two batch instances of $\mathbf{P}^L \mathbf{u}^H$ in the training data and integrate (15) for m timesteps by using the fifth-order ERK method [51] with $\Delta t = 10^{-2}$ over the mesh with the first-order $p = 1$ polynomial and $20 \times 20 \times 20$ elements. In a hexahedral element, the eight nodal points (located at vertices) are used for the first-order discontinuous Galerkin methods. Thus, the degrees of freedom of the input and the output layers in (19) are $n_0 = 40 \times k_w^3$ and $n_D = 40$, respectively. We

¹Q-criterion is defined by $Q = \frac{1}{2} (\|\omega\| - \|\epsilon\|)$, where $\omega_{ij} = \frac{1}{2} \left(\frac{\partial \varphi_i}{\partial x_j} - \frac{\partial \varphi_j}{\partial x_i} \right)$ is vorticity and $\epsilon_{ij} = \frac{1}{2} \left(\frac{\partial \varphi_i}{\partial x_j} + \frac{\partial \varphi_j}{\partial x_i} \right)$ is strain rate. A positive Q value means the relative dominance of the rotational component over the stretching component in the velocity gradient $\nabla \varphi$.

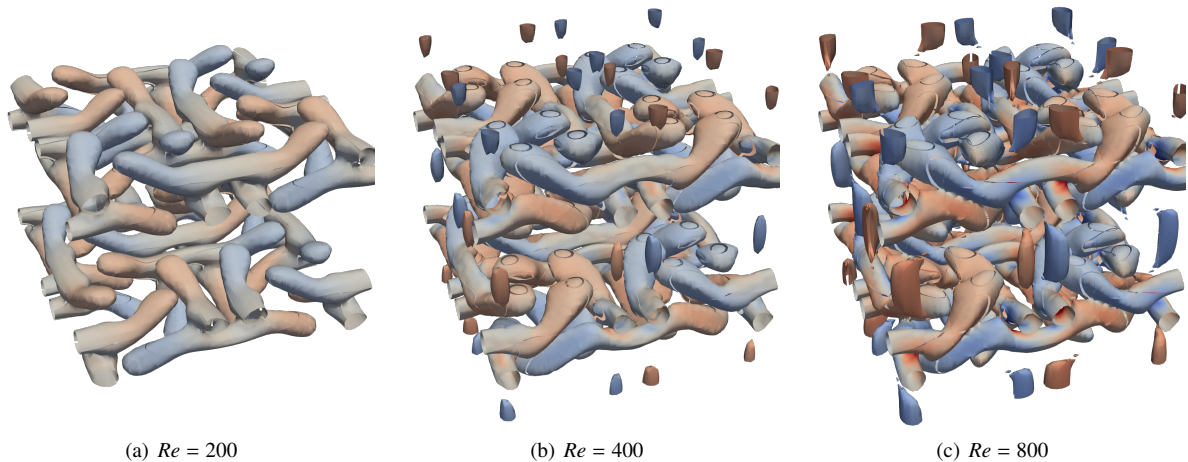


Figure 5: 3D Taylor–Green vortex: Q-criterion isosurfaces for (a) $Re = 200$, (b) $Re = 400$, and (c) $Re = 800$ with $N = 8$ and $10 \times 10 \times 10$ elements at $t = 20$.

take the neural network architecture as $\{n_0, 64, 32, 64, n_D\}$ and train it by using the AdaBelief [52] optimizer with a learning rate of 10^{-3} and 1,000 epochs. The simulation with the same third-order ERK method in different regimes and Re numbers is discussed below.

Results for various time frames at $Re = \{100, 200, 400, 1600\}$

Figure 6 shows the relative error histories of the density, momentum, and total energy for $Re = 100$ with $k_w = 5$ and $m = 11$. Since this flow is in an incompressible regime $M < 0.3$, the fluctuation of the density and the total energy is small. Thus the momentum error is two orders of magnitude larger than that of the density and the total energy. In general, the augmented solution (blue solid line) has smaller relative error than the low-order counterpart (grey dash-dot line). Since the flow starts with smoothed profiles, the difference between the low-order and the augmented solutions is small for $t \in [0, 1]$. All of the filtered, augmented, and low-order solutions are similar to each other at $t = 1$ as shown in Figure 7. As flow evolves, however, the augmented solution shows enhanced accuracy compared with the low-order solution. The momentum error for augmented solutions at $t = 8$ and $t = 15$ is two times smaller than for the low-order counterpart in Figure 6(b). We see the remarkable improvements in the snapshots at $t = 8$ and $t = 15$ in Figure 8 and Figure 9, respectively. The augmented solution successfully recovers the vortical structures, whereas the low-order solution quickly loses the vortices due to the numerical dissipation associated with the low-order solver in the viscous-dominated flows.

We plot the relative error histories of the density, momentum, and total energy for $Re = \{200, 400, 1600\}$ in Figure 10, Figure 11, and Figure 12, respectively. We note that the accuracy of the augmented solutions highly depends on the hyperparameters such as the kernel width k_w and the number of steps m . After conducting a sensitivity study with respect to k_w and m , we choose the best kernel width and the number of steps for each Reynolds number: $k_w = 1$ and $m = 11$ for $Re = 200$, $Re = 400$ and $Re = 1600$. For all the cases with $Re = \{200, 400, 1600\}$, the momentum error dominates over the density and the total energy counterparts, similar to the case with $Re = 100$. For the low-order solution (grey dash-dot line), the relative momentum error grows as the Reynolds number rises. For example, at $t = 15$, the momentum errors of the low-order solution are 1.4×10^{-1} with $Re = 200$ and 3.0×10^{-1} with $Re = 1600$. In comparison with the low-order solution, the augmented solution (blue solid line) has less relative error overall. At $t = 8$, the augmented solutions have almost two times smaller momentum errors than do the low-order solutions for $Re = \{200, 400, 1600\}$. At $t = 15$, the momentum errors of the augmented solution are 6.3×10^{-2} , 1.1×10^{-1} , and 2.0×10^{-1} for $Re = 200$, $Re = 400$, and $Re = 1600$, which are 2.3, 2.0 and 1.5 times smaller than the low-order counterparts, respectively.

Figure 13 and Figure 14 show the snapshots of the filtered, augmented, and low-order solutions for $Re = \{200, 400, 1600\}$ at $t = 8$ and $t = 15$, respectively. With increasing Reynolds number, the flow becomes turbulent, and hence the vortical

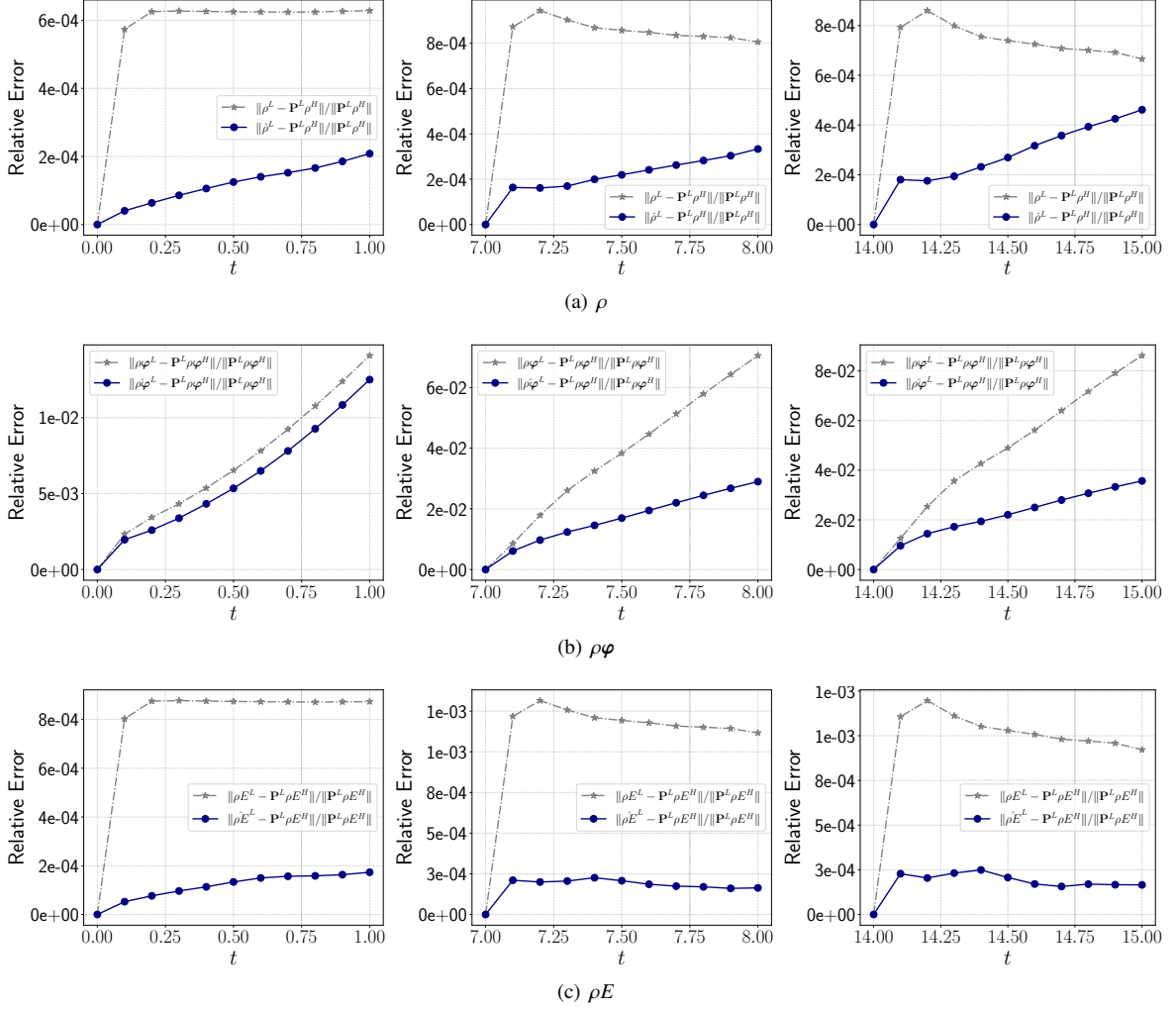


Figure 6: 3D Taylor–Green vortex: error histories of (a) ρ , (b) $\rho\phi$, and (c) ρE for $Re = 100$ with $k_w = 1$ and $m = 11$.

structures are more prevalent because of the mixing. In both figures, the augmented solutions demonstrate significant improvements at $Re = \{200, 400, 1600\}$. Indeed, the neural network source term recovers the missing scales and enhances the accuracy of the low-order approximation.

Sensitivity test for the kernel width k_w and the number of steps m

In this subsection we present a sensitivity study of the prediction of the augmented solution with respect to the kernel width $k_w \in \{1, 3, 5\}$ and the number of steps $m \in \{1, 3, 7, 11\}$ for $Re = 100$ and $Re = 1600$ in Figure 15. Since the momentum error dominates over the density and the total energy counterparts in this example, we show only the momentum errors. We also choose the time interval of $t \in [14, 15]$ because the errors are larger than those of $t \in [0, 1]$ and $t \in [7, 8]$. In general, the relative error decreases with increasing number of steps m , except for some cases. For $Re = 1600$ and $k_w = 5$, $m = 7$ produces smaller error than $m = 11$. Even in these cases, however, $m = 11$ (green solid line) shows better accuracy than $m = 1$ (red dash-dot line). The best cases are $k_w = 5, m = 11$ at $Re = 100$ and $k_w = 1, m = 11$ at $Re = 1600$.² Turbulent flows appear to perform better with single-kernel width for training, but laminar flows appear to perform better with multiple-kernel width.

²At $Re = 100$, the relative error of $k_w = 5, m = 11$ is similar to that of $k_w = 3, m = 11$. $k_w = 5, m = 11$, however, shows better snapshot results than $k_w = 3, m = 11$.

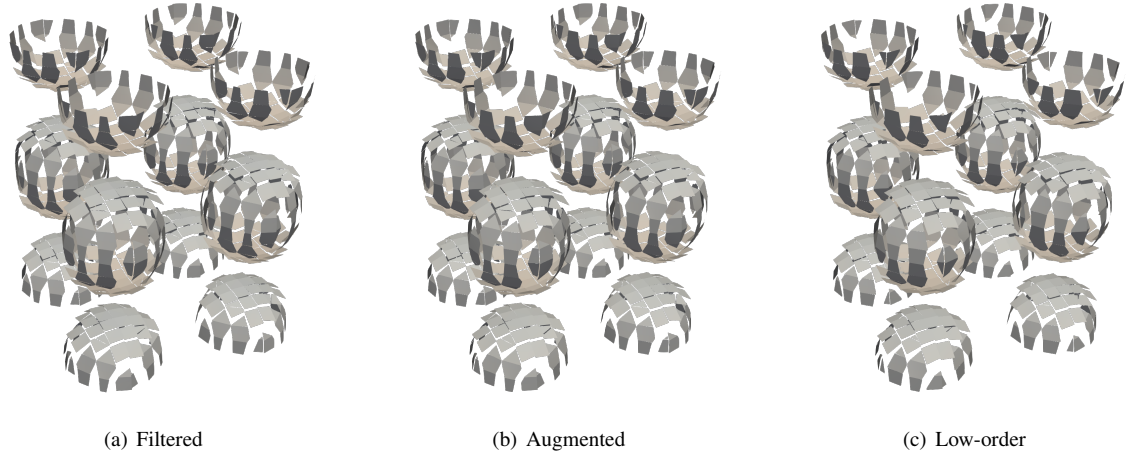


Figure 7: 3D Taylor–Green vortex: Q-criterion isosurfaces for $Re = 100$ for (a) filtered solution, (b) augmented solution, and (c) low-order solution at $t = 1$. The isosurfaces are colored by the z-component of the velocity from -0.1 to 0.1 .

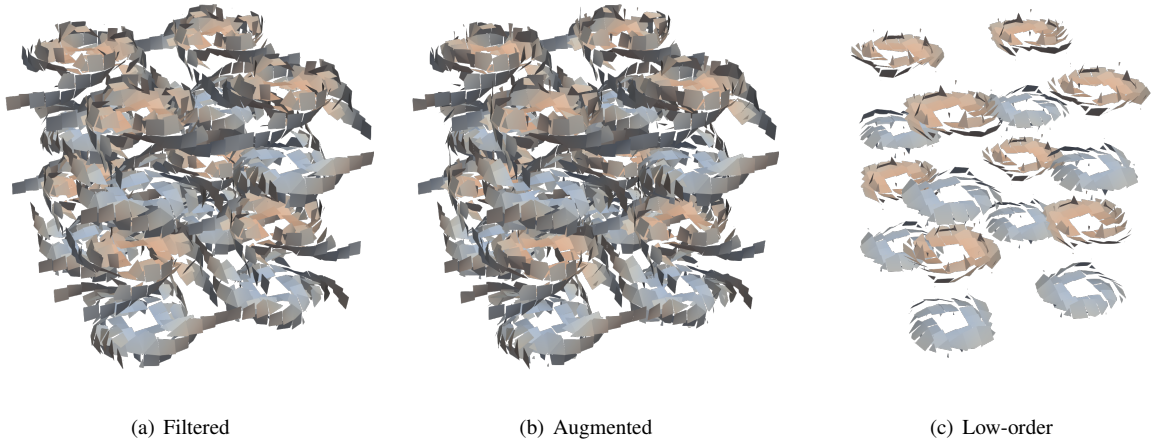


Figure 8: 3D Taylor–Green vortex: Q-criterion isosurfaces for $Re = 100$ for (a) filtered solution, (b) augmented solution, and (c) low-order solution at $t = 8$. The isosurfaces are colored by the z-component of the velocity from -0.1 to 0.1 .

Computational cost

We train the neural network source term and measure the wall-clock times of the prediction of $\hat{\mathbf{u}}^L$, \mathbf{u}^L , and \mathbf{u}^H on ThetaGPU at the Argonne Leadership Computing Facility using a single NVIDIA DGX A100.

For the predictions, we choose the stable timestep size Δt such that doubling the timestep size leads to a blowup. The stable timestep sizes are $\Delta t^H = 10^{-3}$ for high-order solution and $\Delta t^L = 2 \times 10^{-2}$ for low-order and augmented solutions. We make the predictions five times from $t = 14$ to $t = 15$ and report the average wall-clock times in Table 1 for $Re = 100$ and in Table 2 for $Re = 1600$. We denote $\hat{\mathbf{u}}^L$ with $k_w = 1$, $\hat{\mathbf{u}}^L$ with $k_w = 3$, and $\hat{\mathbf{u}}^L$ with $k_w = 5$ by $\hat{\mathbf{u}}^L(k_w = 1)$, $\hat{\mathbf{u}}^L(k_w = 3)$, and $\hat{\mathbf{u}}^L(k_w = 5)$ for brevity. We measure the wall clock twice since JAX has a just-in-time (JIT) compilation. The reason for doing this is that when a function is called for the first time in JAX, it is compiled and the resulting code is cached. As a result, the subsequent run times after the first are significantly faster. We compute JIT compiling time by subtracting the second wall-clock time from the first wall-clock time.

For the JIT compiling time, $\hat{\mathbf{u}}^H$ takes about 2.5 times more time than the others, but \mathbf{u}^L , $\hat{\mathbf{u}}^L(k_w = 1)$, $\hat{\mathbf{u}}^L(k_w = 3)$,

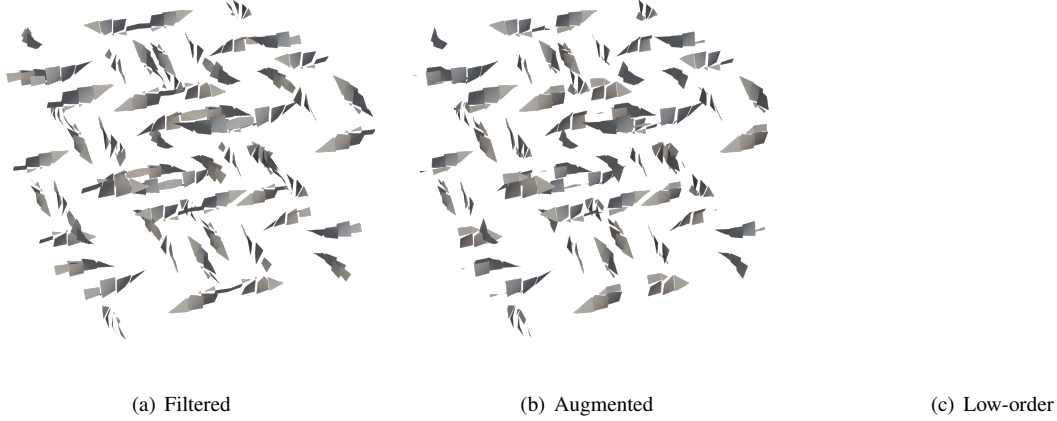


Figure 9: 3D Taylor–Green vortex: Q-criterion isosurfaces for $Re = 100$ for (a) filtered solution, (b) augmented solution, and (c) low-order solution at $t = 15$. The isosurfaces are colored by the z -component of the velocity from -0.1 to 0.1 .

Table 1: 3D Taylor–Green vortex: wall-clock time for the predictions of \mathbf{u}^H , \mathbf{u}^L , and $\hat{\mathbf{u}}^L$ from $t = 14$ to $t = 15$ at $Re = 100$.

	Δt	JIT Compile wc [s]	Simulation wc [s]
\mathbf{u}^H	0.001	47.0	217
\mathbf{u}^L	0.02	17.72	0.35
$\hat{\mathbf{u}}^L(k_w = 1)$	0.02	18.05	0.35
$\hat{\mathbf{u}}^L(k_w = 3)$	0.02	18.04	0.40
$\hat{\mathbf{u}}^L(k_w = 5)$	0.02	18.35	0.51

and $\hat{\mathbf{u}}^L(k_w = 5)$ are comparable to each other. For the second run with a cached code, the wall clock of $\hat{\mathbf{u}}^L(k_w = 1)$ is comparable to that of the low-order solution \mathbf{u}^L . With increasing kernel width k_w , the wall clock of $\hat{\mathbf{u}}^L$ grows. The wall clock of $\hat{\mathbf{u}}^L(k_w = 3)$ is 14% larger than that of $\hat{\mathbf{u}}^L(k_w = 1)$. The wall clock of $\hat{\mathbf{u}}^L(k_w = 5)$ is 48% larger than that of $\hat{\mathbf{u}}^L(k_w = 1)$. This is expected because the input size of the neural network source term increases with increasing the kernel width. The wall clock of the low-order solution \mathbf{u}^L is 620 times smaller than that of the high-order solution \mathbf{u}^H . The augmented solutions $\hat{\mathbf{u}}^L$ with $k_w = 1$, $k_w = 3$, and $k_w = 5$ are about 620, 543, and 425 times faster than the high-order solution \mathbf{u}^H , respectively. Indeed, compared with the high-order solution, the augmented solutions speed up two orders of magnitude. These results provide a significant speedup boost over the one-dimensional cases in [30], where augmenting the neural network source is 3 and 19 times more economical for the one-dimensional convection-diffusion model and the one-dimensional viscous Burgers’ model.

5. Conclusions

In our previous work [30] we presented a methodology for learning subgrid-scale models based on neural ordinary differential equations, where the one-dimensional convection-diffusion equation and viscous Burgers’ equation are discussed in the context of DG methods. In this work we extend our approach to multidimensional compressible Navier–Stokes equations. Our goal is to learn the unresolved scales of the low-order DG solver at a continuous level by utilizing high-order DG simulation data and NODEs. To achieve this goal, we first create a differentiable DG model on a structured mesh for compressible Navier–Stokes equations. Then, we introduce a neural network source term to the spatially discretized DG formulation. In particular, to reduce the size of the neural network parameters, we devise a local neural network source function inspired by the convolutional neural network strategies. The local neural network

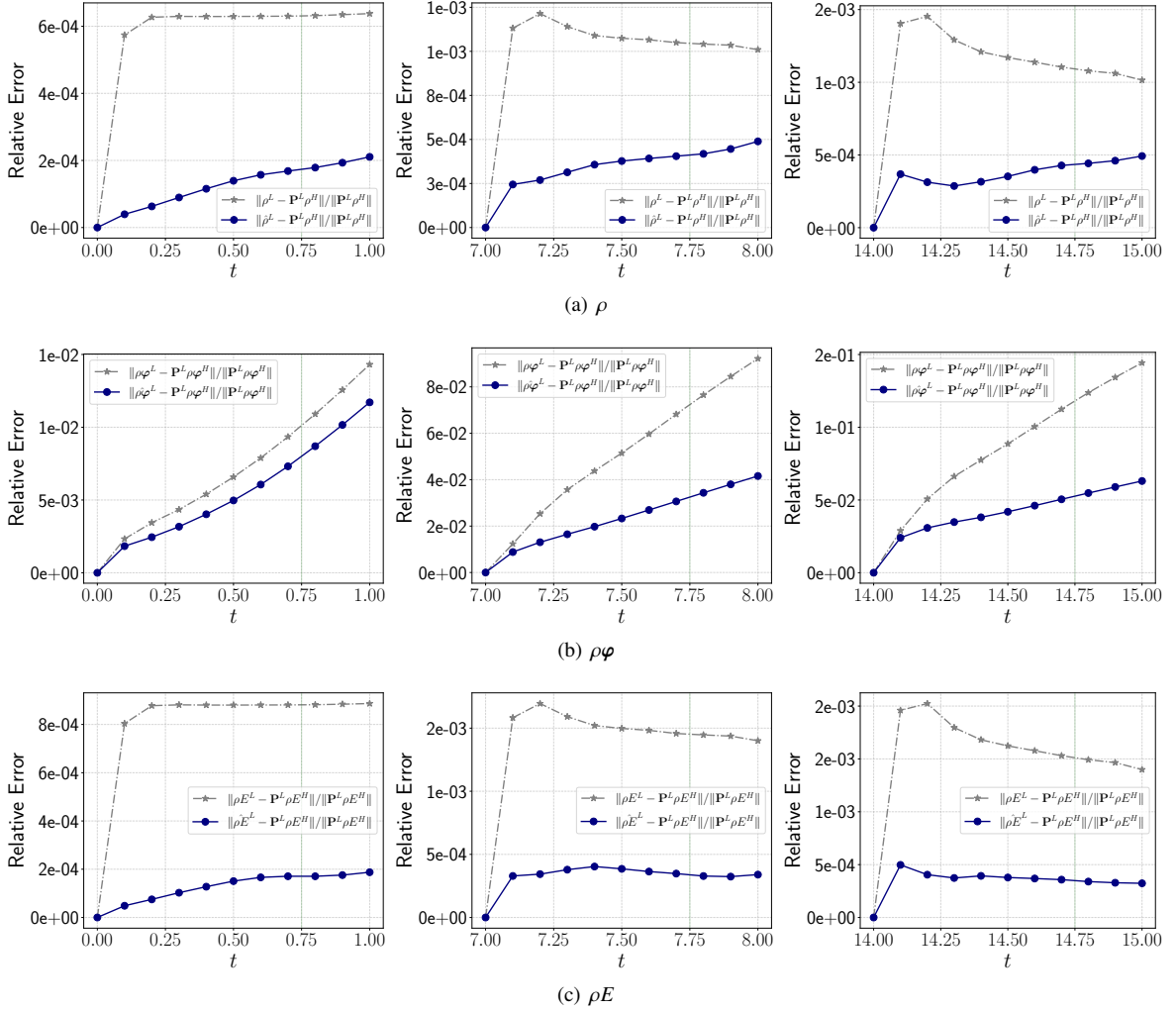


Figure 10: 3D Taylor–Green vortex: error histories of (a) ρ , (b) $\rho\phi$, and (c) ρE for $Re = 200$ with $k_w = 1$ and $m = 11$.

source function, composed of a D -depth feed-forward neural network, slides over the low-order solutions of all the elements and produces a local source approximation for each element. Next, we train the neural network parameters through NODEs. Then, we predict the augmented solution with the neural network augmented DG system with standard timestepping methods such as explicit Runge–Kutta methods. The suggested method learns the continuous source operator for low-order DG solvers to account for the missing scales, predicting a solution with a larger timestep size than that of the high-order DG solvers. This can significantly accelerate the high-order simulation.

We demonstrate the proposed methodology through multidimensional Taylor–Green vortex examples. We consider stable vortices for $t \in [0, 1]$ at $Re = 100$ in the two-dimensional case and various flow regimes with different Reynolds numbers $Re = \{100, 200, 400, 1600\}$ and times $t \in \{[0, 1], [7, 8], [14, 15]\}$ in the three-dimensional case. Augmenting a neural network source term indeed enhances the low-order approximation’s accuracy. In both the two-dimensional and the three-dimensional examples, the augmented solution shows lower error histories of the density, momentum, and total energy than does the low-order solution. In particular, we observe that the augmented solution recovers the missing scales from the low-order solutions, as shown in the snapshots at $t = 8$ and $t = 15$. We also conducted the sensitivity study with respect to the kernel width k_w and the number of steps m . We found that the momentum error tends to decrease as the number of steps increases. Also, it seems that a single local kernel width works better for turbulent than for laminar flows, whereas slightly increasing the kernel width is more appropriate for

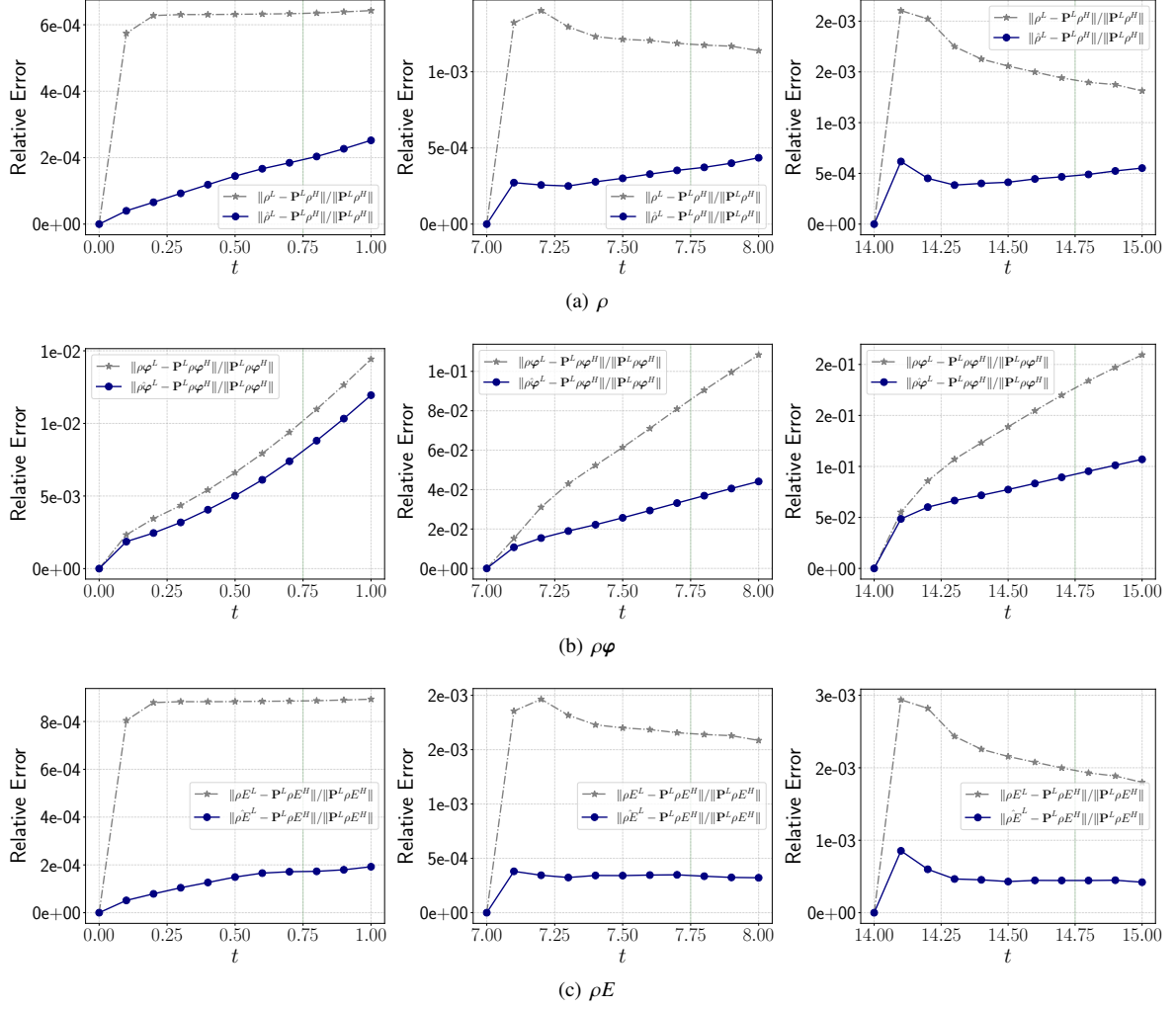


Figure 11: 3D Taylor–Green vortex: error histories of (a) ρ , (b) $\rho\phi$, and (c) ρE for $Re = 400$ with $k_w = 1$ and $m = 11$.

laminar flows than for turbulent flows.

We reported the wall-clock times for the low-order DG approximation, the augmented low-order DG approximation, and the high-order DG approximation. The low-order DG approximation with the neural network source term is 620 times more expensive than the low-order DG approximation. Compared with the high-order DG approximation, the augmented solution is two orders of magnitude faster. With the single-kernel width, the augmented approximation is 620 times more economical than the high-order DG approximation.

Current work successfully demonstrates the potential applicability of employing a neural network source function with the aid of neural ordinary differential equations for multidimensional compressible Navier–Stokes equations. Augmenting the neural network source function not only improves the accuracy of the low-order DG approximation but also significantly speeds up the filtered high-order simulation with a certain degree of precision. Furthermore, we believe that our approach has a benefit for parallel training neural network parameters because DG approaches provide favorable parallel performance and the neural network source function is local. We will investigate this aspect in future work.

Our current approach, however, has limitations. We did not explore complex problems, for which we may need the global neural network source function instead of the local neural network source function. Also, the DG discretization loses the conservation property by introducing the neural network source term. Moreover, the neural network source

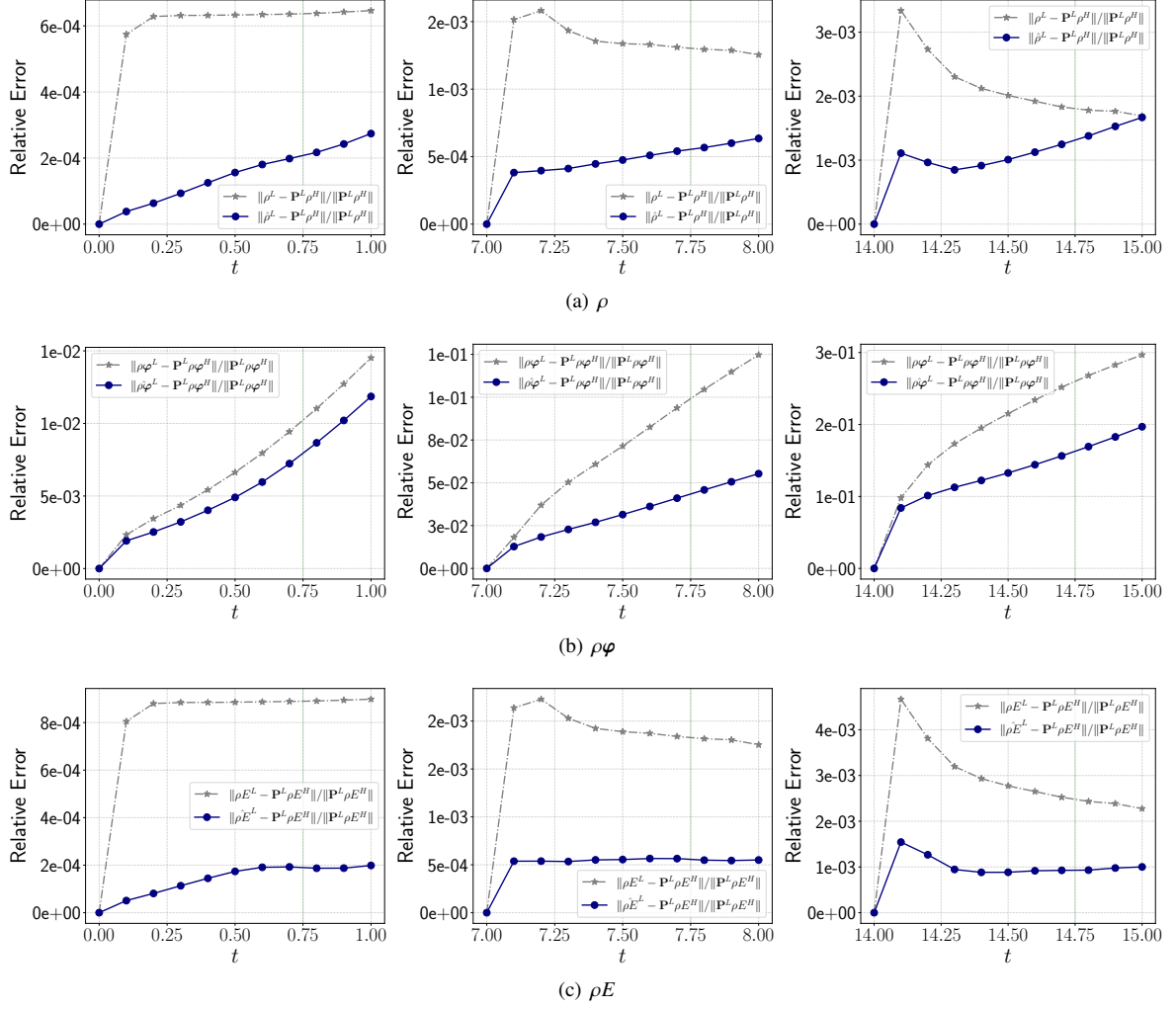


Figure 12: 3D Taylor–Green vortex: error histories of (a) ρ , (b) $\rho\boldsymbol{\varphi}$, and (c) ρE for $Re = 1600$ with $k_w = 1$ and $m = 11$.

function is trained with particular parameters. Therefore, we will explore different neural network architectures that have the potential to alleviate issues with more complex examples.

Appendix A. Compressible Navier–Stokes equations

The homogeneous compressible Navier–Stokes equations in Ω are described by

$$\frac{\partial \rho}{\partial t} + \nabla \cdot (\rho \boldsymbol{\varphi}) = 0, \quad (\text{A.1a})$$

$$\frac{\partial \rho \boldsymbol{\varphi}}{\partial t} + \nabla \cdot (\rho \boldsymbol{\varphi} \otimes \boldsymbol{\varphi} + \mathcal{I} p) = \nabla \cdot \boldsymbol{\sigma}, \quad (\text{A.1b})$$

$$\frac{\partial \rho E}{\partial t} + \nabla \cdot (\rho \boldsymbol{\varphi} H) = \nabla \cdot (\boldsymbol{\sigma} \boldsymbol{\varphi}) - \nabla \cdot \Pi, \quad (\text{A.1c})$$

where ρ is the density [kg m^{-3}]; $\boldsymbol{\varphi}$ is the velocity vector [m s^{-1}];³ p is the pressure [N m^{-2}]; $\rho E = \rho e + \frac{1}{2} \rho \|\boldsymbol{\varphi}\|^2$ is the total energy [J m^{-3}]; $e = \frac{p}{\rho(\gamma-1)}$ is the internal energy [J kg^{-1}]; $H = E + \frac{p}{\rho} = \frac{a^2}{\gamma-1} + \frac{1}{2} \|\boldsymbol{\varphi}\|^2$ is the total specific

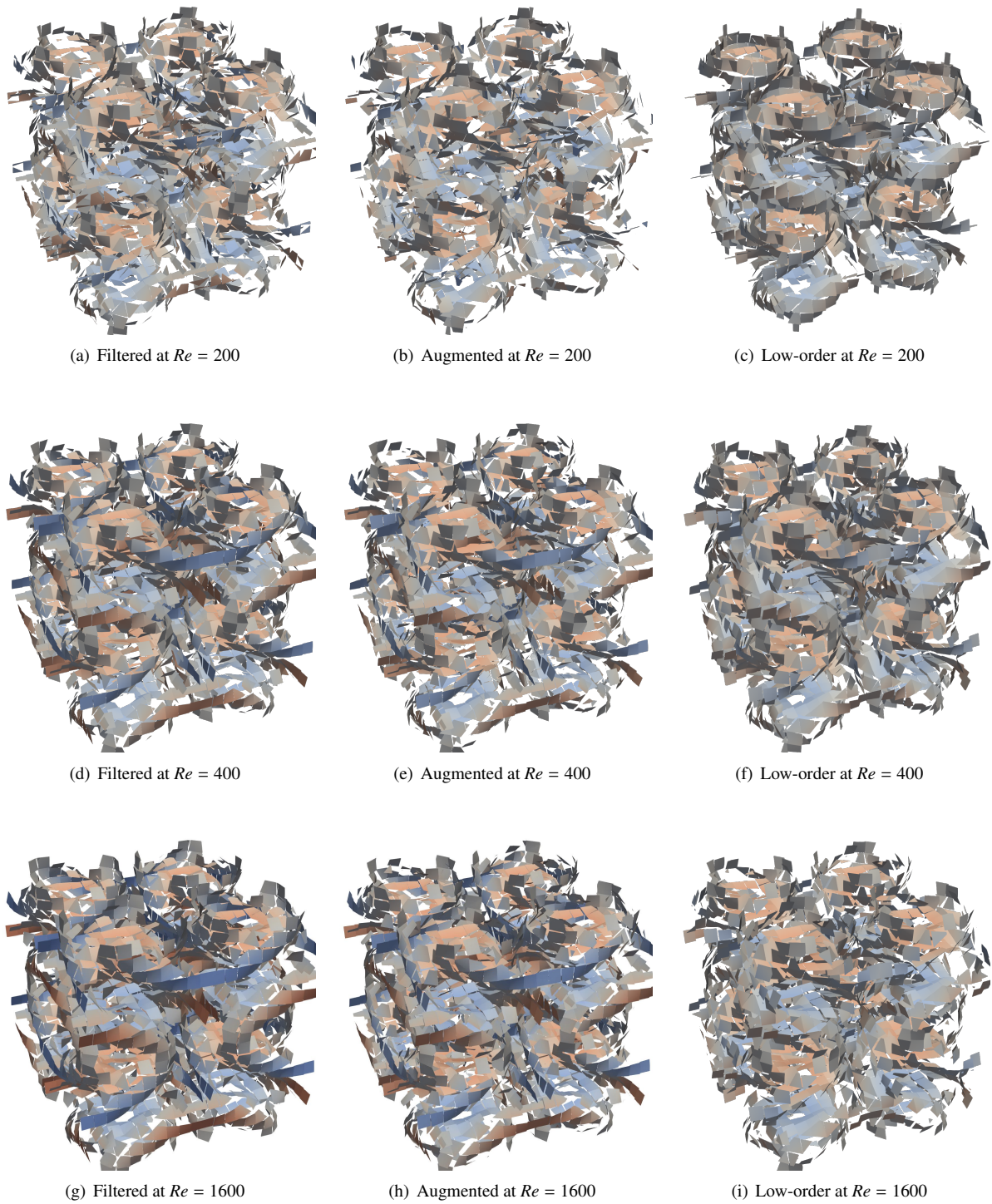


Figure 13: 3D Taylor–Green vortex: Q-criterion isosurfaces for $Re = \{200, 400, 1600\}$ for (a) filtered solution, (b) augmented solution, and (c) low-order solution at $t = 8$. The isosurfaces are colored by the z-component of the velocity from -0.1 to 0.1 .

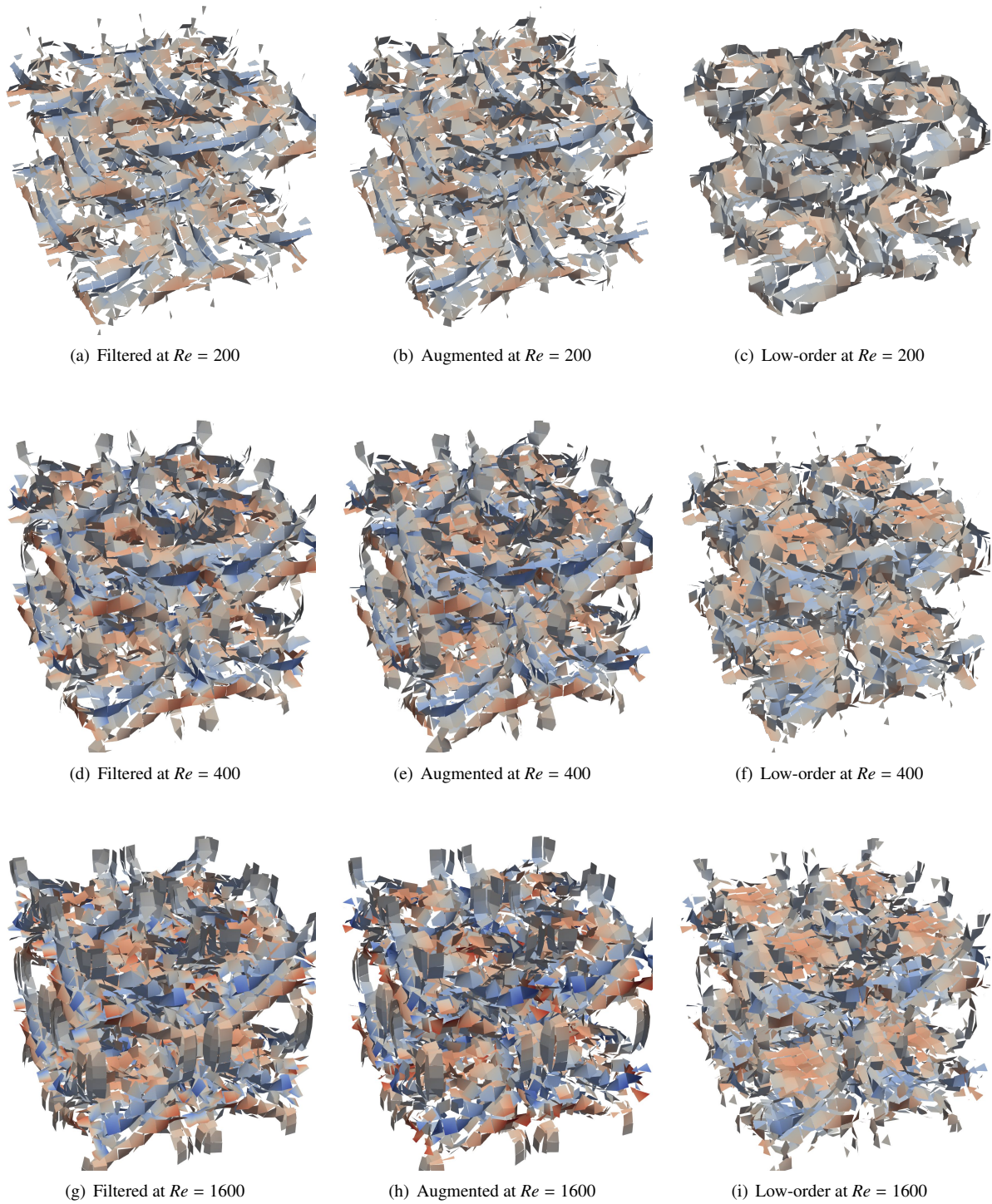


Figure 14: 3D Taylor–Green vortex: Q-criterion isosurfaces for $Re = \{200, 400, 1600\}$ for (a) filtered solution, (b) augmented solution, and (c) low-order solution at $t = 15$. The isosurfaces are colored by the z-component of the velocity from -0.1 to 0.1 .

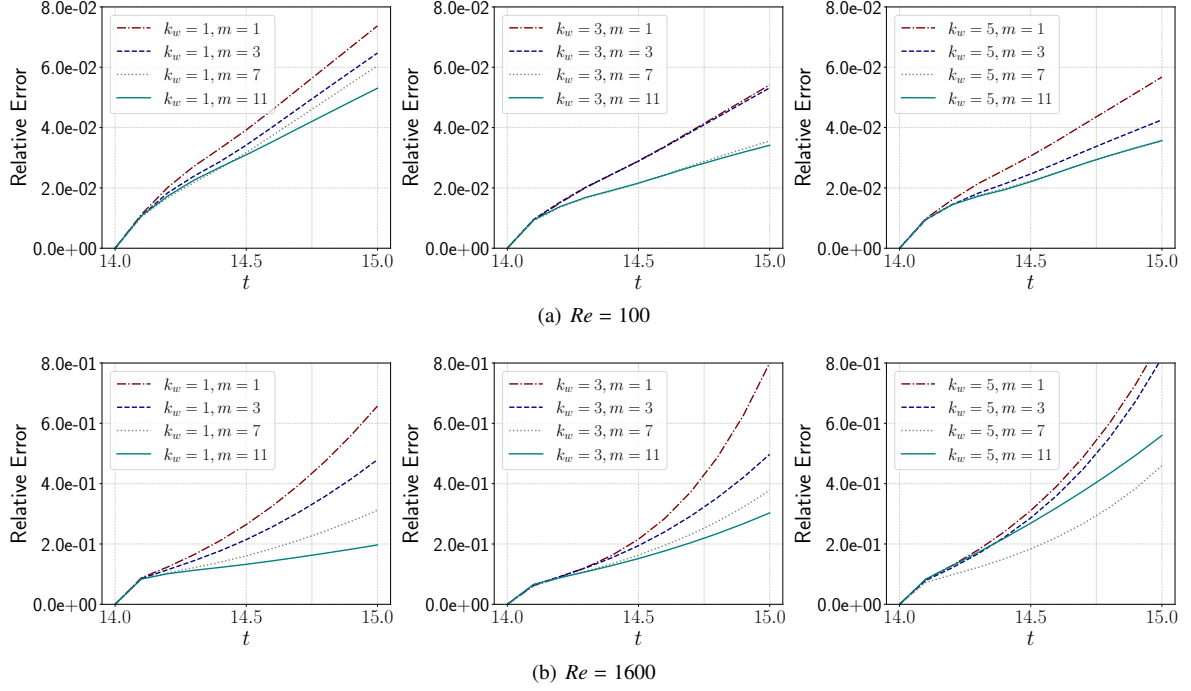


Figure 15: 3D Taylor–Green vortex: error histories of $\hat{\rho}\hat{\varphi}$ for $Re \in \{100, 1600\}$ with respect to the number of steps m .

Table 2: 3D Taylor–Green vortex: wall-clock time for the predictions of \mathbf{u}^H , \mathbf{u}^L , and $\hat{\mathbf{u}}^L$ from $t = 14$ to $t = 15$ at $Re = 1600$.

	Δt	JIT Compile wc [s]	Simulation wc [s]
\mathbf{u}^H	0.001	47.4	217
\mathbf{u}^L	0.02	17.83	0.33
$\hat{\mathbf{u}}^L(k_w = 1)$	0.02	18.56	0.36
$\hat{\mathbf{u}}^L(k_w = 3)$	0.02	18.11	0.39
$\hat{\mathbf{u}}^L(k_w = 5)$	0.02	18.53	0.49

enthalpy [J kg^{-1}]; $\sigma = \mu(\nabla\boldsymbol{\varphi} + \nabla(\boldsymbol{\varphi})^T - \frac{2}{3}\mathcal{I}\nabla \cdot \boldsymbol{\varphi})$ is the viscous stress tensor; $\Pi = -\kappa\nabla T$ is the heat flux; T_m is the temperature; $\kappa = \mu c_p Pr^{-1}$ is the heat conductivity [$\text{W m}^{-1} \text{K}^{-1}$]; μ is the dynamic viscosity [Pa s]; Pr is the Prandtl number; $a = (\gamma p \rho^{-1})^{\frac{1}{2}}$ is the sound speed [m s^{-1}] for an ideal gas; $\gamma = c_p c_v^{-1}$ is the ratio of the specific heats; and c_p and c_v are the specific heat capacities at constant pressure and at constant volume [$\text{J kg}^{-1} \text{K}^{-1}$], respectively.

By the nondimensionalized variables using the speed of sound as a reference velocity,

$$\rho^* = \frac{\rho}{\rho_\infty}, p^* = \frac{p}{\rho_\infty a_\infty^2}, \boldsymbol{\varphi}^* = \frac{\boldsymbol{\varphi}}{a_\infty}, x^* = \frac{x}{L}, t^* = \frac{t}{L/a_\infty}, \mu^* = \frac{\mu}{\mu_\infty}, \text{ and } T^* = \frac{T}{T_\infty},$$

we rewrite the governing equation (A.1) as

$$\frac{\partial \rho^*}{\partial t^*} + \nabla^* \cdot (\rho^* \boldsymbol{\varphi}^*) = 0, \quad (\text{A.2a})$$

$$\frac{\partial \rho \boldsymbol{\varphi}^*}{\partial t^*} + \nabla^* \cdot (\rho \boldsymbol{\varphi}^* \otimes \boldsymbol{\varphi}^* + \mathcal{I} p^*) = \nabla^* \cdot \boldsymbol{\sigma}^*, \quad (\text{A.2b})$$

$$\frac{\partial \rho E^*}{\partial t^*} + \nabla^* \cdot (\rho \boldsymbol{\varphi}^* H^*) = \nabla^* \cdot (\boldsymbol{\sigma}^* \boldsymbol{\varphi}^*) - \nabla^* \cdot \Pi^*, \quad (\text{A.2c})$$

where $\sigma^* = \tilde{\mu} (\nabla^* \boldsymbol{\varphi}^* + \nabla^* (\boldsymbol{\varphi}^*)^T - \frac{2}{3} \mathcal{I} \nabla^* \cdot \boldsymbol{\varphi}^*)$, $\Pi^* = -\frac{\tilde{c}_p \tilde{\mu}}{Pr} \nabla^* T^*$, $\nabla^* = \frac{1}{L} \nabla$, $\tilde{\mu} = \frac{\mu^* M_\infty}{Re_\infty}$, $Re_\infty = \frac{\rho_\infty u_\infty L}{\mu_\infty}$, $M_\infty = \frac{u_\infty}{a_\infty}$, and $\tilde{c}_p := \frac{1}{\gamma-1}$. The normalized equation of state for an ideal gas is $p^* = \gamma^{-1} \rho^* T^* = \rho^* e^* (\gamma - 1)$. Sutherland's formula is $\mu^* = (T^*)^{\frac{3}{2}} \frac{1 + \frac{su}{T_\infty}}{T^* + \frac{su}{T_\infty}}$ with $su = 110.4$ K. In this study, we use the nondimensionalized form (A.2), and we omit the superscript (*).

Acknowledgments

This material is based upon work supported by the U.S. Department of Energy, Office of Science, Office of Advanced Scientific Computing Research (ASCR) program. We also gratefully acknowledge the use of ThetaGPU and Polaris in the resources of the Argonne Leadership Computing Facility, which is a DOE Office of Science User Facility supported under Contract DE-AC02-06CH11357.

- [1] W. H. Reed, T. R. Hill, Triangular mesh methods for the neutron transport equation, Los Alamos Report LA-UR-73-479.
- [2] B. Cockburn, G. E. Karniadakis, C.-W. Shu, The development of discontinuous Galerkin methods, in: *Discontinuous Galerkin methods: theory, computation and applications*, Springer, 2000, pp. 3–50.
- [3] D. N. Arnold, F. Brezzi, B. Cockburn, L. D. Marini, Unified analysis of discontinuous Galerkin methods for elliptic problems, *SIAM Journal on Numerical Analysis* 39 (5) (2002) 1749–1779.
- [4] T. Bui-Thanh, O. Ghattas, Analysis of an hp-nonconforming discontinuous Galerkin spectral element method for wave propagation, *SIAM Journal on Numerical Analysis* 50 (3) (2012) 1801–1826.
- [5] J. Rudi, A. C. I. Malossi, T. Isaac, G. Stadler, M. Gurnis, P. W. Staar, Y. Ineichen, C. Bekas, A. Curioni, O. Ghattas, An extreme-scale implicit solver for complex PDEs: highly heterogeneous flow in earth's mantle, in: *Proceedings of the International Conference for High Performance Computing, Networking, Storage and Analysis*, 2015, pp. 1–12.
- [6] S. Kang, T. Bui-Thanh, A scalable exponential-DG approach for nonlinear conservation laws: With application to Burger and Euler equations, *Computer Methods in Applied Mechanics and Engineering* 385 (2021) 114031.
- [7] F. M. de Lara, E. Ferrer, Accelerating high order discontinuous Galerkin solvers using neural networks: 3D compressible Navier-Stokes equations, *Journal of Computational Physics* (2023) 112253.
- [8] P. Sagaut, M. Germano, On the filtering paradigm for LES of flows with discontinuities, *Journal of Turbulence* (6) (2005) N23.
- [9] A. D. Beck, D. G. Flad, C. Tonhäuser, G. Gassner, C.-D. Munz, On the influence of polynomial de-aliasing on subgrid scale models, *Flow, Turbulence and Combustion* 97 (2016) 475–511.
- [10] J. Smagorinsky, General circulation experiments with the primitive equations: I. the basic experiment, *Monthly Weather Review* 91 (3) (1963) 99–164.
- [11] M. Germano, U. Piomelli, P. Moin, W. H. Cabot, A dynamic subgrid-scale eddy viscosity model, *Physics of Fluids A: Fluid Dynamics* 3 (7) (1991) 1760–1765.
- [12] S. Collis, The DG/VMS method for unified turbulence simulation, in: *32nd AIAA Fluid Dynamics Conference and Exhibit*, 2002, p. 3124.
- [13] K. Sengupta, F. Mashayek, G. Jacobs, Large-eddy simulation using a discontinuous Galerkin spectral element method, in: *45th AIAA Aerospace Sciences Meeting and Exhibit*, 2007, p. 402.
- [14] U. Piomelli, T. A. Zang, Large-eddy simulation of transitional channel flow, *Computer Physics Communications* 65 (1-3) (1991) 224–230.
- [15] S. Liu, C. Meneveau, J. Katz, On the properties of similarity subgrid-scale models as deduced from measurements in a turbulent jet, *Journal of Fluid Mechanics* 275 (1994) 83–119.
- [16] C. Meneveau, J. Katz, Scale-invariance and turbulence models for large-eddy simulation, *Annual Review of Fluid Mechanics* 32 (1) (2000) 1–32.
- [17] J. P. Boris, On large eddy simulation using subgrid turbulence models comment 1, in: *Whither Turbulence? Turbulence at the Crossroads: Proceedings of a Workshop Held at Cornell University, Ithaca, NY, March 22–24, 1989*, Springer, 2005, pp. 344–353.
- [18] A. Uranga, P.-O. Persson, M. Drela, J. Peraire, Implicit large eddy simulation of transition to turbulence at low Reynolds numbers using a discontinuous Galerkin method, *International Journal for Numerical Methods in Engineering* 87 (1-5) (2011) 232–261.
- [19] G. J. Gassner, A. D. Beck, On the accuracy of high-order discretizations for underresolved turbulence simulations, *Theoretical and Computational Fluid Dynamics* 27 (3-4) (2013) 221–237.
- [20] J. S. Hesthaven, T. Warburton, *Nodal discontinuous Galerkin methods: Algorithms, Analysis, and Applications*, Springer Science & Business Media, 2007.
- [21] J. Viquerat, P. Meliga, A. Larcher, E. Hachem, A review on deep reinforcement learning for fluid mechanics: An update, *Physics of Fluids* 34 (11).
- [22] R. Vinuesa, S. L. Brunton, Enhancing computational fluid dynamics with machine learning, *Nature Computational Science* 2 (6) (2022) 358–366.
- [23] M. A. Mendez, A. Ianiro, B. R. Noack, S. L. Brunton, *Data-Driven Fluid Mechanics: Combining First Principles and Machine Learning*, Cambridge University Press, 2023.
- [24] D. Kochkov, J. A. Smith, A. Alieva, Q. Wang, M. P. Brenner, S. Hoyer, Machine learning-accelerated computational fluid dynamics, *Proceedings of the National Academy of Sciences* 118 (21) (2021) e2101784118.
- [25] K. Duraisamy, Perspectives on machine learning-augmented Reynolds-averaged and large eddy simulation models of turbulence, *Physical Review Fluids* 6 (5) (2021) 050504.
- [26] K. Fukami, K. Fukagata, K. Taira, Machine-learning-based spatio-temporal super resolution reconstruction of turbulent flows, *Journal of Fluid Mechanics* 909 (2021) A9.

- [27] A. Beck, D. Flad, C.-D. Munz, Deep neural networks for data-driven LES closure models, *Journal of Computational Physics* 398 (2019) 108910.
- [28] F. Manrique de Lara, E. Ferrer, Accelerating high order discontinuous Galerkin solvers using neural networks: 1D Burgers' equation, *Computers & Fluids* 235 (2022) 105274.
- [29] F. Manrique de Lara, E. Ferrer, Accelerating high order discontinuous Galerkin solvers using neural networks: 3D compressible Navier–Stokes equations, arXiv:2207.11571v1 [physics.flu-dyn].
- [30] S. Kang, E. M. Constantinescu, Learning subgrid-scale models with neural ordinary differential equations, *Computers & Fluids* 261 (2023) 105919.
- [31] R. T. Chen, Y. Rubanova, J. Bettencourt, D. K. Duvenaud, Neural ordinary differential equations, *Advances in Neural Information Processing Systems* 31.
- [32] K. He, X. Zhang, S. Ren, J. Sun, Deep residual learning for image recognition, in: *Proceedings of the IEEE conference on Computer Vision and Pattern Recognition*, 2016, pp. 770–778.
- [33] B. Avelin, K. Nyström, Neural ODEs as the deep limit of ResNets with constant weights, *Analysis and Applications* 19 (03) (2021) 397–437.
- [34] R. Gupta, P. Srijith, S. Desai, Galaxy morphology classification using neural ordinary differential equations, *Astronomy and Computing* 38 (2022) 100543.
- [35] Y. Rubanova, R. T. Chen, D. Duvenaud, Latent ODEs for irregularly-sampled time series, *Advances in Neural Information Processing Systems*, 2019.
- [36] J. R. Dormand, P. J. Prince, A family of embedded Runge–Kutta formulae, *Journal of Computational and Applied Mathematics* 6 (1) (1980) 19–26.
- [37] L. S. Pontryagin, *Mathematical theory of optimal processes*, CRC press, 1987.
- [38] J. Zhuang, N. Dvornek, X. Li, S. Tatikonda, X. Papademetris, J. Duncan, Adaptive checkpoint adjoint method for gradient estimation in neural ODE, in: *International Conference on Machine Learning*, PMLR, 2020, pp. 11639–11649.
- [39] C. Rackauckas, Y. Ma, J. Martensen, C. Warner, K. Zubov, R. Supekar, D. Skinner, A. Ramadhan, A. Edelman, Universal differential equations for scientific machine learning, arXiv:2001.04385v4 [cs.LG].
- [40] Z. Huang, S. Liang, H. Zhang, H. Yang, L. Lin, Accelerating numerical solvers for large-scale simulation of dynamical system via NeurVec, arXiv:2208.03680v1 [cs.CE].
- [41] V. Shankar, R. Maulik, V. Viswanathan, Differentiable Turbulence II, arXiv preprint arXiv:2307.13533.
- [42] D. A. Kopriva, *Implementing spectral methods for partial differential equations: Algorithms for scientists and engineers*, Springer Science & Business Media, 2009.
- [43] A. Fabra, J. Baiges, R. Codina, Finite element approximation of wave problems with correcting terms based on training artificial neural networks with fine solutions, *Computer Methods in Applied Mechanics and Engineering* 399 (2022) 115280.
- [44] V. Nair, G. E. Hinton, Rectified linear units improve restricted Boltzmann machines, in: *Proceedings of the 27th International Conference on Machine Learning*, 2010, pp. 807–814.
- [45] J. Bradbury, R. Frostig, P. Hawkins, M. J. Johnson, C. Leary, D. Maclaurin, G. Necula, A. Paszke, J. VanderPlas, S. Wanderman-Milne, Q. Zhang, JAX: composable transformations of Python+NumPy programs (2018).
- [46] M. Hessel, D. Budden, F. Viola, M. Rosca, E. Sezener, T. Hennigan, Optax: composable gradient transformation and optimisation, in JAX, Github: Deepmind 2 (2020) 980–1080.
- [47] P. Kidger, C. Garcia, Equinox: neural networks in JAX via callable PyTrees and filtered transformations, *Differentiable Programming workshop at Neural Information Processing Systems* 2021.
- [48] P. Kidger, On neural differential equations, arXiv:2202.02435v1 [cs.LG].
- [49] B. Cockburn, C.-W. Shu, The local discontinuous Galerkin method for time-dependent convection-diffusion systems, *SIAM Journal on Numerical Analysis* 35 (6) (1998) 2440–2463.
- [50] G. I. Taylor, A. E. Green, Mechanism of the production of small eddies from large ones, *Proceedings of the Royal Society of London. Series A-Mathematical and Physical Sciences* 158 (895) (1937) 499–521.
- [51] C. Tsitouras, Runge–Kutta pairs of order 5 (4) satisfying only the first column simplifying assumption, *Computers & Mathematics with Applications* 62 (2) (2011) 770–775.
- [52] J. Zhuang, T. Tang, Y. Ding, S. C. Tatikonda, N. Dvornek, X. Papademetris, J. Duncan, Adabelief optimizer: Adapting stepsizes by the belief in observed gradients, *Advances in Neural Information Processing Systems* 33 (2020) 18795–18806.

Government License (will be removed at publication): The submitted manuscript has been created by UChicago Argonne, LLC, Operator of Argonne National Laboratory ("Argonne"). Argonne, a U.S. Department of Energy Office of Science laboratory, is operated under Contract No. DE-AC02-06CH11357. The U.S. Government retains for itself, and others acting on its behalf, a paid-up nonexclusive, irrevocable worldwide license in said article to reproduce, prepare derivative works, distribute copies to the public, and perform publicly and display publicly, by or on behalf of the Government. The Department of Energy will provide public access to these results of federally sponsored research in accordance with the DOE Public Access Plan. <http://energy.gov/downloads/doe-public-access-plan>.